High-resolution morpho-sedimentary and paleoenvironmental evolution of Akka Wadi (Drâa Basin, Morocco) from Late Pleistocene to Holocene

Fatima Saadi, Larbi Boudad, Maïlys Richard, Jean-François Berger

High-resolution morpho-sedimentary and paleoenvironmental evolution of Wadi Akka (Drâa Basin, Morocco) from the late Pleistocene to the Holocene.

Fatima Saadi [a,b,*], **Larbi Boudad** [a], **Mailys Richard** [c,d], **Jean-François Berger** [b]

[a] *Geosciences, Water, Environment Laboratory, Earth Sciences Department, Faculty of Sciences, Mohammed V University in Rabat, 4 Avenue Ibn Battouta P.O. Box 1014, Rabat, Morocco.*
[b] *CNRS, UMR 5600 EVS-IRG, University of Lyon. 18 Rue Chevreul, 69362 Lyon CEDEX 07, UMR 5600, France.*
[c] *Archéosciences Bordeaux, UMR 6034 CNRS-Bordeaux Montaigne University, Pessac, France.*
[d] *Department of Early Prehistory and Quaternary Ecology, University of Tübingen, Tübingen, Germany.*

* Corresponding author : Fatima SAADI <fatima_saadi@um5.ac.ma>

Abstract

The fluvial evolution of southern Morocco during the Late Quaternary, particularly in non-Mediterranean basins such as the Wadi Akka, a tributary of the Drâa, remains poorly documented. This study presents the first chronostratigraphic framework for the Wadi Akka formations, based on a high-resolution reconstruction of fluvial dynamics and paleoenvironmental changes since the end of the last interglacial period. The analysis follows a multiproxy approach, combining geomorphological, sedimentological, and geochemical data, and is supported by 13 radiocarbon and four optically stimulated luminescence (OSL) ages. Nine main stratigraphic units reveal alternating phases of aggradation, pedosedimentary stability, and incision, associated with climatic fluctuations from Marine Isotope Stage (MIS) 5b (~82 ka) to the late Holocene. During MIS 3 (~40 ka cal BP), a low-energy hydromorphic environment prevailed, marked by fine sedimenta-tion and soil development under relatively humid conditions. The early African Humid Period (11.400-9.700 cal BP) is characterized by fluvio-lacustrine settings, peat layers, and tufa deposits, indicating stable, wet environments. Conversely, arid phases are marked by signifi-cant incision and sedimentary hiatuses, particularly between 9.500-8.500 and after 6.000 cal BP. Alluviation phases are also dated to around 7 200 and 656-579 cal BP. The presence of tuf deposits and travertine dams indicates peaks in humidity, especially during the beginning of Little Ice Age. Finally, comparison with other regional archives has allowed for the reconstruction of Upper Pleistocene and Holocene paleoenvironmental conditions at both regional and supra-regional scales, highlighting the correspondence between phases recorded in the Akka Plain and broader climatic events in the region.

Keywords:

Fluvial geomorphology, multi-proxy analysis, MIS 5b and MIS 3, Holocene, Akka Plain, Drâa Valley.

1. Introduction

The glacial periods of the Late Quaternary, particularly Marine Isotope Stages (MIS) 5b and 3, as well as the Holocene interglacial, reflect the complex processes underlying Earth's climatic variability (Siddall et al., 2006; Romero et al., 2011; Bereiter et al., 2012). These periods are characterized by alternating wet and dry phases, which continue to be the focus of extensive research aimed at understanding the origins and driving mechanisms of these climatic shifts (Foley et al., 2003; Castañeda et al., 2009; Specht et al., 2024; Zaky et al., 2024). During the early Holocene, substantial evidence indicates significantly increased moisture levels across the Sahara Desert in North Africa (Petit-Maire & Riser, 1981 ;Petit-Maire & Riser, 1983 ; Pachur et al., 1987 ; Petit-Maire, 1989 ; ; Pachur & Hoelzmann, 1991 ; Depreux et al., 2021; Petit-Maire, 2021 ; Cheddadi et al., 2021;). Geomorphological, lacustrine, and paleoecological records consistently show that the region was markedly wetter than today and extensively vegetated throughout the early to mid-Holocene. This multi-millennial phase of enhanced humidity is commonly referred to as the "African Humid Period" or the "Green Sahara" ; Street-Perrott et al., 1993 ;Kröpelin et al., 2008; Lézine et al., 2011; Limondin-Lozouet et al., 2013 ; Burrough & Thomas, 2013 Campbell et al., 2017 Depreux et al., 2022 ; Lghamour et al., 2024). Furthermore, the northward expansion of the African monsoon brought abundant rainfall to areas that are now arid, transforming the Sahara into a verdant landscape dotted with lakes, rivers, and vegetation ranging from wooded steppe to savanna (Petit-Maire & Riser, 1981 ;Petit-Maire & Riser, 1983). Pollen analyses have revealed the presence of tropical and Sahelian taxa, indicating increased biodiversity. In addition, speleothem records confirm the persistence of humid conditions during the Late Pleistocene and early Holocene (Ritchie et al., 1985; Salzmann & Waller, 1998; Lézine & Casanova, 1989; Cheddadi et al., 2009; Brahim et al., 2023; Helmens, 2014 ; Lézine et al., 2023 ; Paine et al., 2024). However, as summer insolation gradually declined, the African monsoon retreated southward, leading to progressive aridification and the re-establishment of desert conditions across the Sahara (Nicole Petit-Maire et al., 1983; Salzmann & Waller, 1998) . This process of desertification is well documented during the mid-Holocene, particularly through lacustrine records such as those from Lake Yoa in Chad, which reveal a continuous and gradual drying trend over the past 6,000 years (Kröpelin et al., 2008). An abrupt increase in Saharan dust deposition in the Atlantic around 5,000 cal BP further supports this shift (Demenocal et al., 2000). Marine sediment records also confirm this trend, as shown by the studies of Lézine et al.(2005), Weldeab et al. (2005), and Haslett & Smart (2006).

Despite these climatic evidence, research on the evolution of fluvial systems in North Africa remains limited. Yet, alluvial archives represent valuable indirect indicators of paleohydrological dynamics during the Late Pleistocene and Holocene. Unlike slope or colluvial deposits, which reflect more localized processes, fluvial records integrate environmental changes across entire watersheds, offering

a broader and more comprehensive perspective on past hydrological variability (Faust et al., 2004; Zielhofer & Faust, 2008; Zielhofer et al., 2008).

This transitional period is crucial for understanding the profound landscape transformations and the multiple forcing mechanisms that have driven the ongoing aridification of North Africa. However, the current state of research highlights significant gaps, as many regions still lack chronological frameworks or pedo-sedimentary archives documenting paleoenvironmental, climatic, and anthropogenic events during the Late Quaternary. In southern Morocco, the Akka Wadi is a major right-bank tributary of the Drâa River in its lower basin, which spans approximately 66 km² and extends into the northwestern Sahara Desert. The history of studies on this sector of Africa has received little attention from geomorphologists and Quaternary scientists. Notably, the Akka Plain has never been investigated in the context of Holocene paleoenvironmental reconstructions. This area of south-eastern Morocco lacks of absolute chronological data, despite a few earlier contributions (Weisrock et al., 1991; Wengler et al., 2002; Mathieu et al., 2004; Weisrock et al., 2006 , 2008) . As a result, there remains a significant gap in morpho-pedosedimentary and paleoenvironmental documentation of climatic and anthropogenic changes during the recent Quaternary (Mathieu et al., 2004). In contrast, only a handful of recent studies have focused on marine sequences off Cape Ghir in southern Morocco (Baqloul et al., 2021; Tadoumant et al., 2022). Meanwhile, the Mediterranean watersheds of northern Morocco, such as the Moulouya River and its tributaries, as well as the Kert River, have been the focus of extensive geomorphological and paleoenvironmental research. (Lefèvre, 1985; El Amrani et al., 2008; Zielhofer et al., 2010; Ibouhouten et al., 2010; Bartz et al., 2018 ; Depreux et al, 2021, 2022), resulting in a robust and near-continuous Holocene chronostratigraphic framework for that region.

The main objectives of this study are as follows; a) to carry out a comprehensive geomorphological analysis of alluvial formations across several sectors of the Akka Basin, b) to refine the chronostratigraphic framework of recent Quaternary alluvial deposits through the examination of multiple transects and the application of absolute dating methods, including radiocarbon (^{14}C) and optically stimulated luminescence (OSL), c) to perform detailed physico-chemical and sedimentological analyses on samples collected from selected profiles, with the aim of developing a diachronic model reconstructing the hydro-geomorphological and paleoenvironmental evolution of the region, d) to investigate the climatic and anthropogenic drivers of the observed paleoenvironmental changes in the Akka sequence by comparing our results with published paleoclimatic and paleoenvironmental data at the regional scale, encompassing the north-western Sahara and broader North Africa.

2. Study area

The Akka Wadi is a major right-bank tributary of the Drâa River (Figure. 1a), situated in the pre-Saharan zone of the Western Anti-Atlas in southern Morocco. It drains a sub-basin covering approximately 2.190

km² along a course of about 100 km (Figure. 1b). Due to its geographical position, the Tata-Akka region experiences a continental Saharan hyper-arid climate. Annual precipitation is low, averaging around 100 mm (Monographie 2015 – Agence du Bassin Hydraulique Drâa), primarily occurring as intense thunderstorms. Prolonged dry spells of 4 to 5 months without rainfall are common. Temperatures exhibit considerable daily and seasonal variability, ranging from minima of around 12 °C in winter to highest values reaching 49 °C in summer.

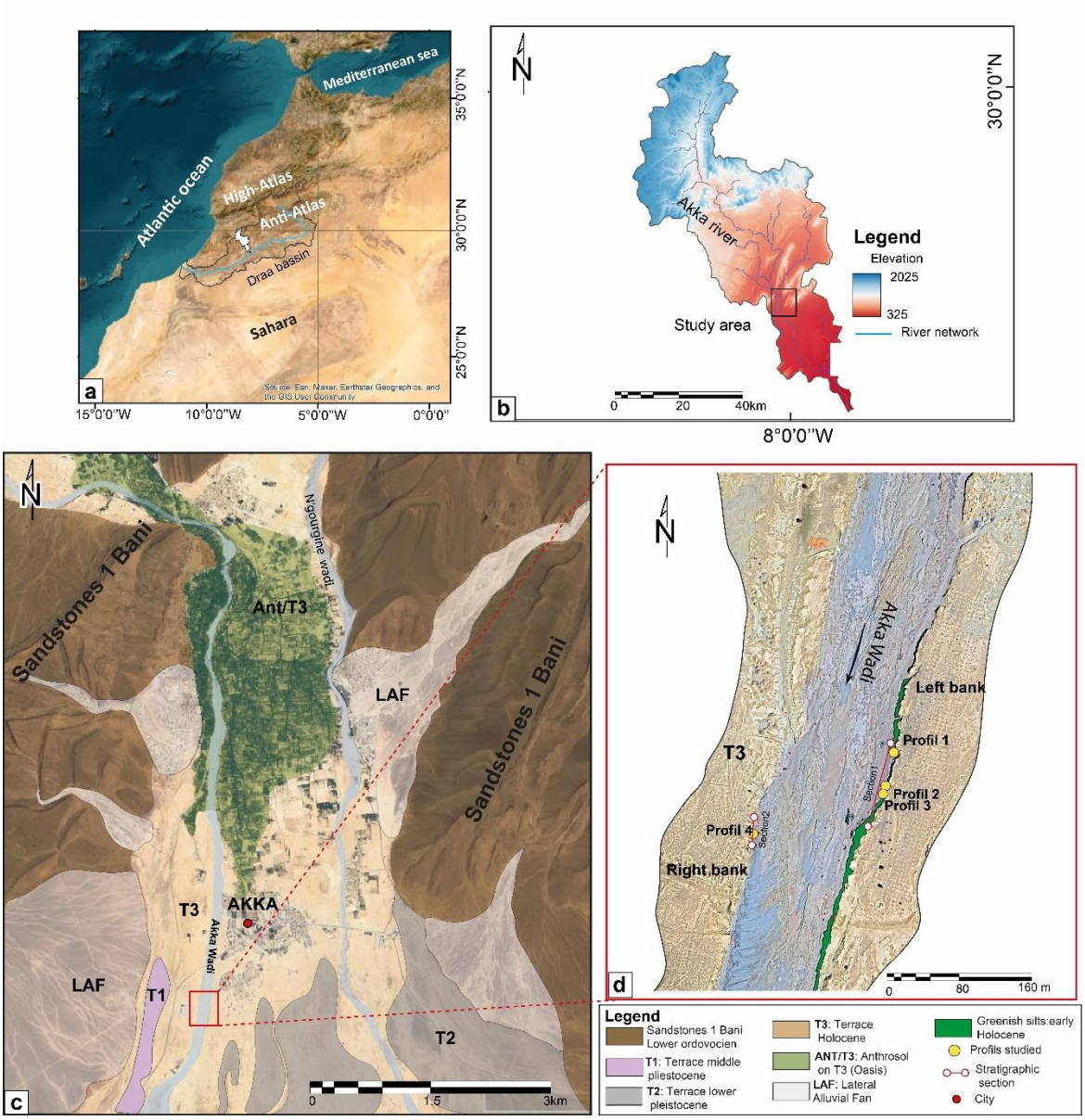

Figure. 1*. Geographical location of the study area: a) Satellite image of Morocco showing the Akka sub-basin (outlined in white) within the Drâa basin (outlined in black). (Source: Terra Color imagery, Esri, 2009), b) Topographical map of the Akka watershed highlighting the study area. (Source: Shuttle Radar Topography Mission (SRTM)), c) Geological and geomorphological map of the Akka plain with the study area indicated by a*

red rectangle. The legend below corresponds to maps (c) and (d), d) Locations of the profiles and stratigraphic sections studied along the eastern and western banks of the wadi.

3. Materials and methods

3.1 Geomorphological and Chronostratigraphic Context

The identification of the studied terraces is based on a geomorphological survey combining the analysis of Google Earth satellite images and field observations. Satellite images allowed the identification of the best-preserved Holocene alluvial terraces, while field campaigns validated these observations by identifying the most intact construction sections, exposed by the recent natural incision of watercourses. Four field campaigns were thus conducted in the Akka region, southern Morocco, in May 2022, April 2023, November 2023, and January 2024.

The geomorphological map of the Akka area (Figure. 1c) illustrates the geological and morphological framework of the study site. The upstream watershed is dominated by rugged mountainous terrain reaching approximately 1100 m in altitude, characterized by steep slopes composed of ancient Ordovician rocks, notably the Bani sandstones. Downstream, the landscape extends into low alluvial desert plains, rich in pebbles, up to the confluence of the Wadi Akka with the Drâa River (Figure 1b).

The oldest terraces, T1 and T2 (Figure. 1c), consist of gravel formations attributed to the Middle to Upper Pleistocene, as indicated by the geological map of the Western Anti-Atlas and the Drâa Plains (Akka–Tafagount–Tata) (Choubert & Ennadifi, 1970). These two terraces were not investigated in the field due to the absence of precise chronological constraints but are included here for contextual purposes. The most recent terrace, T3, where the studied outcrops are located, is composed of fluviolacustrine deposits and more or less bedded floodplain silts, very locally interrupted by gravel layers with a thickness of 5 to 6 meters. These sediments, mainly greenish silts and occasional tufa deposits, are attributed to the Holocene (Choubert & Ennadifi, 1970). Below the T3 terrace lies the Ant/T3 terrace (Figure. 1c,d), which is topographically lower and corresponds to anthrosol deposits linked to the establishment of the Akka oasis, a topic that will be addressed in more detail later.

Two stratigraphic sections were studied on the recent T3 terrace. The first section, (Figures 2a and 2b), located on the left bank of the Akka wadi (29°22'50.66"N/8°15'51.25"O), includes three profiles (profiles 1, 2, and 3) arranged from north to south. The second section, located on the right bank (29°22'47.40"N/ 8°15'57.39"O), contains a fourth profile (profile 4). These profiles were selected based on the clear continuity of the sedimentary layers, which is essential for accurate stratigraphic interpretation. The lithostratigraphic analysis of the four profiles led to the identification of 21 sedimentary units.

The identification of sedimentary units is primarily based on lithological descriptions carried out in the field, including outcrop sketches, as well as the analysis of structures, texture, and color of the units.

Due to local topographic configurations, successive interbedding of alluvial layers, oblique intersections of old palaeochannels, observable truncations, and longitudinal facies variations, it is often necessary to study several complementary sedimentary logs at the same site. This approach makes it possible to best reconstruct the alluvial archive, to capture its initial geometry by developing a local master core that is representative of all the hydro-geomorphological and sedimentary events recorded in the stratigraphic sequence.

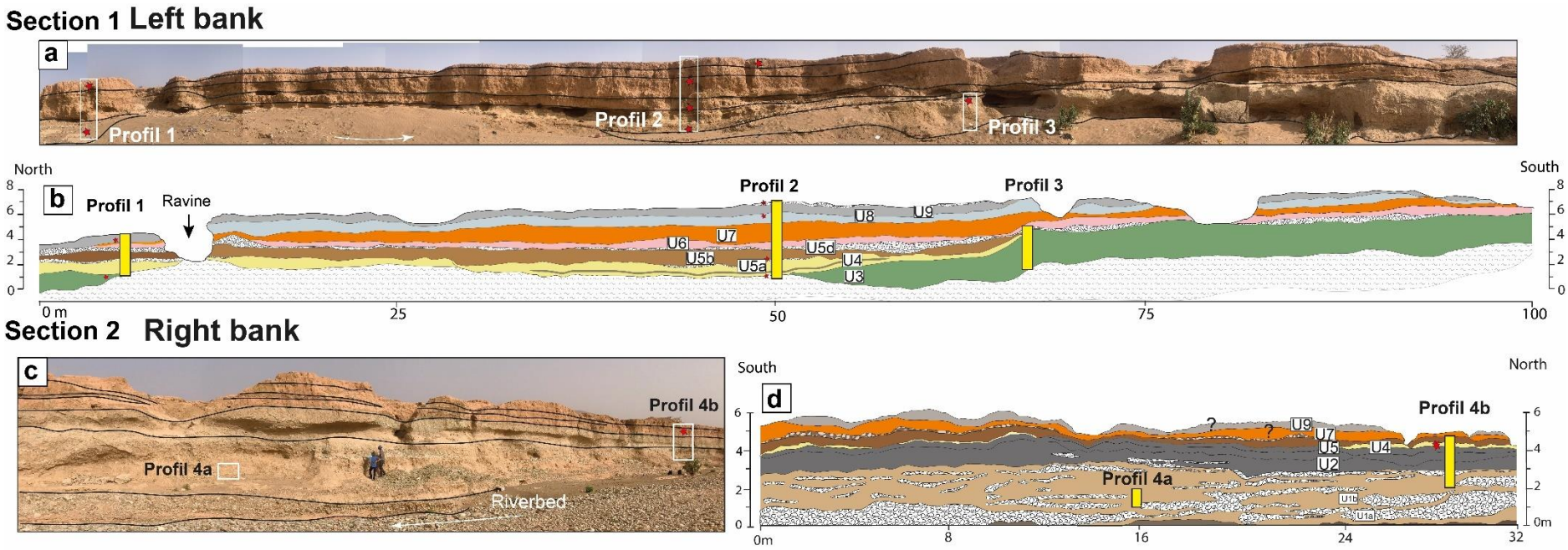

Figure. 2*. a) Panoramic photograph of the left bank outcrop of Akka Wadi; b) Stratigraphic section of the left bank showing the location of the three studied stratigraphic profiles (1, 2, and 3), c) Panoramic photograph of the right bank outcrop of Akka Wadi, d) Stratigraphic section of the right bank with the location of the studied profiles (4a and 4b),*

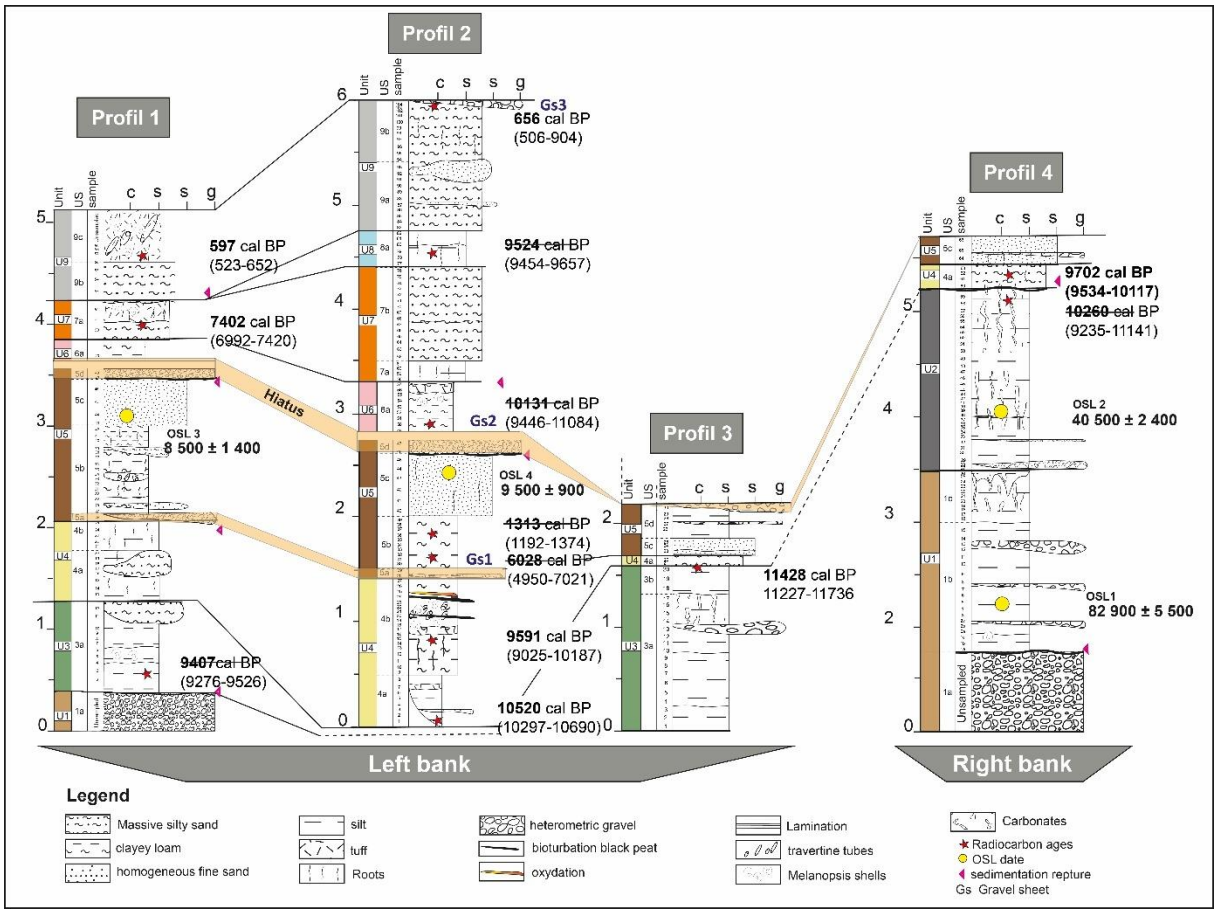

Figure 3 : Correlation of the four dated stratigraphic sequences. (The crossed-out dates indicate a chronostratigraphic inconsistency)

Figure 3 shows a lithostratigraphic correlation of the various units and sub-units from the studied profiles on both sides of the Akka wadi. The four profiles reveal eight broadly comparable pedosedimentary phases on both banks, along with significant morphological changes in the alluvial plain, related to successive incision and refill events. While the two stratigraphic sections are easily accessible for sampling, the scarcity or absence of carbonized remains, especially throughout the coarse basal unit (U1) and the subsequent unit (U2), led us to complement radiocarbon dating with the luminescence dating method, as a complementary technique for the parts where radiocarbon dating material is not available. A detailed description each of these main units is provided in Section 4.2.

3.2 Sedimentological and pedological analysis

Sediment samples of approximately 200 g were systematically collected at regular intervals of 4 to 6 cm by recovering material in bulk (using a trowel or pick from the walls of the natural section, thereby destroying the sedimentary structure), based on the lithostratigraphic variations observed in the field . A total of 259 samples were collected from the four sequences. according to the chronostratigraphic order of the master core created. These samples underwent a multiproxy analysis in the laboratory, following a systematic stratified approach, including geochemistry, sedimentology, and chronology.

3.3 Chronology

3.3.1 Radiocarbon dating

The chronology of the studied sequences is based on 13 AMS radiocarbon ages obtained from charcoal and organic matter (mineralized peat). Due to the scarcity of carbonaceous material, more than 45 samples sieved through a 200-micron mesh (>50), followed by binocular examination at magnifications up to 50x in both natural and incident light to better identify carbonized micro-debris. Despite using AMS, many carbonized micro-fragments had to be combined to reach the required 1 to 2 mg for dating. We sometimes had to group 2 samples 6cm apart, but always included in the same stratigraphic sub-unit. This methodological approach ensures that all collected material comes from the same stratigraphic unit. The obtained ages were then assessed for chronostratigraphic consistency, and any date showing inconsistency was systematically excluded in order to ensure the robustness of the proposed chronological framework. The AMS analyses were performed at the Poznań laboratories (Poland). Dates were calibrated using IntCal20 (Reimer et al., 2020) with Calib 8 software. Radiocarbon dating results are presented in Table 1.

3.3.2 Optically Stimulated Luminescence (OSL) and Post-Infrared Stimulated Luminescence (pIRIR) Dating:

Four blocks were collected from the two studied sections for luminescence dating of sediments. On the left bank, sample AKKA2-OSL1 (profile 4) was taken at a depth of 225 cm, while AKKA2-OSL2 (profile 4) comes from a level at 380 cm. On the right bank, AKKA2-OSL3 (profile 1) was collected at a depth of 250 cm, and AK-KA2-OSL4 (profile 2) at 280 cm.

a- **Sample preparation**

The samples were prepared at the Archéosciences Bordeaux laboratory (Bordeaux Montaigne University, France), under subdued red light and controlled conditions in order to prevent light exposure. The core of the blocks was extracted and prepared for luminescence analyses. The external part of the blocks, which was exposed to light during sampling, was kept for dose rate measurements.

For luminescence dating analyses, each sample was sieved with water and the 100-140 µm fraction was chemically treated following published protocols (e.g. Tribolo et al., 2013) including HCl (10%) to dissolve the carbonates and H2O2 (30%) to degrade the organic matter. The quartz and feldspars were extracted using density separation with heavy liquid (heteropoly tung-state of sodium). Three separations were conducted, the first one to extract heavy minerals (d=2.72 g/cm3), the second one to separate quartz and feldspars (d=2.62 g/cm3) and the third one to separate plagioclase and potassium feldspars (d=2.58 g/cm3). The quartz fraction was then treated using H2SiF6 (31%) over one week and rinsed with HCl (10%) to eliminate the possi-ble remaining feldspars.

For dose rate measurements, the external part of each block was dried in an oven and the difference between the wet and the dry weight was used to calculate the water content. Note that due to the warm conditions at the time of the sampling, the samples were almost dried and the measured water content may not reflect the average water content during burial time. The ages were thus calculated assuming a water content of 6%. This fraction was then sealed in a container that was analysed using a laboratory gamma-ray spectrometer equipped with a high-resolution, broad energy Ge (BEGe) detector to determine the U, Th, and K content in each sample and derive the beta dose rate. The gam-ma dose rate was measured *in situ* using a portable gamma-ray spectrometer connected to a LaBr probe (Inspector 1000, Canberra) at the same location as the samples. The data were treated using the "threshold" technique (Mercier & Falguères, 2007). The cosmic dose rate was calculated taking into account the current depth of the samples following the equation in Prescott & Hutton, (1988)

a- **Luminescence measurements**

Multi-grain (MG) analyses were first conducted on the quartz of the four samples (1 mm ø aliquots) using the protocol given in Tab. S1 with a TL/OSL Lexsyg Smart reader (Richter et al., 2015) and a Lexsyg Research reader (Richter et al., 2013). The OSL signal was integrated using the first 1.5 seconds and the back-ground subtracted using the last 20 seconds, and the signal was detected with a combination of UV filters (Schott BG-3, 3 mm in conjunction with a Delta BP365/50 EX). Dose recovery tests (DRT) were con-ducted on MG quartz aliquots in order to assess the reliability of the protocol. The disks were bleached two minutes in a solar simulator (Hönle 500) and a given dose of 266 Gy (AKKA2-OSL1), 202 Gy (AKKA2-OSL2), and 91 Gy (AKKA2-OSL3) was applied before applying the single aliquot regeneration (SAR) protocol in Tab. S1. The preheat temperature was fixed at 240°C (AKKA2-OSL1, 2 and 3) and 260°C (AKKA2-OSL1 and 3), and three aliquots were measured for each tempera-ture. The DRT (recovered/given) values are, for AKKA2-OSL 1, 0.76 ± 15% (240°C) and 0.75 ± 3% (260°C); for AKKA2-OSL 2, 0.95 ± 3% (240°C); for AKKA2-OSL3, 0.94 ± 5% (240°C) and 0.95 ± 10% (260°C). However, considering that the OSL signal of AKKA2-OSL1 was close to saturation and that the DRT values were under the commonly accepted range for MG aliquots of 1 ± 10%, the post-infrared infrared stimulated luminescence protocol at 290°C ($pIRIR_{290}$, Thiel et al., 2011) was ap-plied on K-feldspars (supplementary Tab. S2) using a TL/OSL Lexsyg Smart reader. The IRSL signal was detected with a combination of optical filters (Schott BG 39-3 mm; AHF Brightline HC 414/46-3.5 mm). For the other samples, some of the quartz DRCs were saturated or close to saturation (OSL 2 and 3) and high overdispersion (OD) values were obtained (21%, 34% and 55% for AKKA2-OSL2, 3 and 4 respectively), probably due to differential bleaching (see details in the results section). Single grain (SG) OSL analyses were thus performed using the protocol displayed in Tab. S3 on a Risø OSL/TL reader. A green laser was used to measure 1000 grains and the signal was detected using Hoya U340 filters. DRT tests were conducted on SG disks for AK-KA2-OSL 2 (given dose = 147 Gy) and 3 (given dose = 69 Gy) using the protocol in Tab. S3. The recovered/given values are 0.99 ± 15% (AKKA2-OSL2) and 1.18 ± 20%

(AKKA2-OSL3). These ratios are included within 1 ± 20%, due to the intrinsic variations of the samples at the single grain scale. The equivalent doses obtained using both single and multi-grain measurements were selected using the following criteria: a recycling ratio limit of 10%; a recuperation <5% of the natural signal; a maximum test dose error of 10%; and a test dose signal >3 sigma above background. The MG pIRIR290 signal was integrated using the first 5 seconds and the back-ground subtracted using the last 50 seconds. The SG OSL signal was integrated using the first 0.07 seconds and the background subtracted using the last 0.25 sec-onds. The DRC were obtained using an exponential + linear function for the pIRIR290 measurements and an exponential function for the OSL measurements.

3.3.3 Sedimentological and geochemical analyses:

The sedimentological and geochemical analyses presented in this study were conducted on the OMEAA platform of UMR 5600 – EVS (Environment, City, Society) at the Université Lumière Lyon

a. Laser Granulometry

Grain size analysis was carried out to measure the size of sediment particles and to assess the energy required for their transport. The method is based on measuring laser beam diffraction and the light intensity scattered by particles smaller than 2 mm. Measurements were performed using a Fritsch Analysette 22 laser granulometer.

Prior to laser granulometry, the samples were chemically pretreated: several treatments with H_2O_2 to remove organic matter, and with HCl to dissolve carbonates, followed by deflocculation with KCl. After rinsing and centrifugation, the samples were dispersed in a sodium hexametaphosphate solution. This method enables the evaluation of flow energy by reconstructing transport hydrodynamics and provides a precise characterization of clay (0.4–2 µm), silt (2–63 µm), and sand (63 µm–2 mm) fractions, as well as variations in hydrological regimes over time. Data processing was performed using the Gradistat software (version 8), developed in Excel by Simon J. Blott and Kenneth Pye (Blott & Pye, 2001). The D50 and D90 values were used to assess flow energy: D50 represents the median flow value, while D90 indicates the maximum flow energy (Passega, 1964; Bravard, 1983). Although D99 would more accurately represent the maximum competence of the current responsible for particle transport (Salvador, 2016), the data curves did not allow reliable determination of D99 values, so D90 was preferred instead.

b. Loss on Ignition (LOI)

The loss on ignition (LOI) method was used to determine the organic matter (OM) and carbonate ($CaCO_3$) content of 259 samples. Samples were first dried at 106°C for 24 hours. Organic matter content was then measured by calcining the dried, ground samples at 550°C for 4 hours using a Nabertherm

muffle furnace,while carbonate content was determined by firing the samples at 950°C for 2 hours (Heiri et al., 2001).

c. ***Volume Magnetic Susceptibility (MS)***

Magnetic susceptibility provides insights into the composition and origin of sediments, as well as the post-depositional processes they may have undergone, particularly pedogenesis. This parameter is highly dependent on the chemical and mineralogical composition of the sediments, notably the presence of minerals sensitive to magnetic fields—especially iron-bearing phases such as ferrimagnetic minerals (iron oxides, hydroxides, and oxyhydroxides) (Dearing, 1999).

At a local scale, magnetic susceptibility can also be influenced by various environmental and diagenetic processes, including redox conditions associated with fluctuations in the water table, pedogenic processes involving the alteration, mobilization, and concentration of iron compounds by microbial and bacterial activity, bioturbation, physico-chemical weathering (e.g., hydrolysis), secondary processes following erosion and transport, and even the impact of fire on soil surfaces (Mullins, 1977).

Measurements were conducted on oven-dried and finely ground samples to minimize grain-size effects. Samples were placed in plastic cups and analyzed using a Bartington MS2E dual-frequency sensor operating at 4.65 kHz, with a sensitivity range of 0.1 and a measurement period of 15 seconds. Each sample was measured in triplicate, and the mean value was recorded following the protocol established by Dearing (1999). Results are expressed in SI units (10^{-8} m^3/kg).

d. ***Geochemical Analysis and Principal Component Analysis (PCA)***

X-ray fluorescence can be used to approximate the geochemical composition of sediment through the detection of a number of major and minor elements. To analyze the geochemical content of the three alluvial sequences studied, we used aportable Nikon XRF spectrometer. which can measure the quantities of forty major and minor elements. Data quality in terms of data precision was analyzed by performing triplicate measurements. Samples, previously dried and ground, were placed in cups covered with a film to minimize interference from factors such as grain size, porosity, and moisture content (Profe et al., 2016).

The geochemical data were analyzed by establishing correlation curves between stratigraphic logs and measured elemental concentrations to identify those showing significant variations. Only the elements Mn, Al, Fe, K, Rb, Ti, Si, Zr, Sr, S, Cr, Mg, and Ca were selected for their consistent detection above limits and meaningful variability. Several geochemical ratios were used to evaluate flow energy and redox conditions. The Zr/Rb ratio serves as an indicator of flooding and coarser (sandy) alluvial deposits in a fluvial context (Rothwell & Croudace, 2015; Jones et al., 2012; Wang et al., 2011). The Fe/Mn ratio help in assessing the redox conditions of the alluvial plain (Rothwell & Croudace, 2015), while the

Ca/Mg ratio indicates biochemical calcite precipitation related to low environmental hydrodynamics (Lauterbach et al., 2011). The Si/Al ratio is used to identify the origin of windblown or sediment dust (Klasen et al., 2015; Zech et al., 2008; Profe et al., 2016) and is correlated with other proxies influenced by grain size (Liang et al., 2013). Lastly, the Rb/Sr ratio serves as an indicator of soil weathering and/or erosion of developed soils (Jones et al., 2012; Rothwell & Croudace, 2015; Profe et al., 2016).

To synthesize geochemical data signal, a Principal Component Analysis (PCA) was conducted. Only the eleven most relevant elements—Rb, Fe, Ti, K, Al, Mg, Si, Zr, S, Mn, and Ca—were included in the PCA, based on their environmental interpretability and local stratigraphic relevance. The analysis was performed in R using the FactoMineR, package. No standardization was applied, as all variables were expressed in comparable intensity units derived from the XRF measurements. The PCA was based on a correlation matrix (default in FactoMineR), and no missing values were present in the selected dataset.

4. Results and Interpretations

4.1 Chronological Results :

4.1.1 Radiocarbon Dating

Radiocarbon dating provided a total of 13 ages on organic material (charcoal and organic matter). Of these, six dates were excluded because they were inconsistent with the chronostratigraphic framework established in the field. These discrepancies appear to be mainly due to contamination by older material, likely reintroduced as a result of repeated phases of erosion and alluviation upstream of the site a common process in fluvial contexts.

***Table 1**; Chronological data of samples from the Wadi Akka: conventional radiocarbon ages and calibrated ages.*

Sample	Laboratory code	Depth (cm)	Material	C14 (BP)	Age (cal BP)	Median (BP, 2σ)
Aka2_log1_0bas	Poz-168159	5	Peat	9320 ± 60	10297-10690	10520
Aka2_log1_14	Poz-168169	75	Charcoal	8560 ± 230	9025-10187	9591
Aka2_log1_31	Poz-168161	160	Charcoal	5270 ± 460	4950-7021	6028
Aka2-P1-51	Poz-182377	180	Charcoal	6290 ±80	6992-7420	7204
Aka2_log1_49	Poz-168162	290	Charcoal	9010 ± 310	9446-11084	10131
Aka2_log3_78	Poz-168164	450	Charcoal	8550 ± 50	9454-9657	9524
Aka2_log3_102	Poz-168165	590	Charcoal	700 ± 120	506-904	656
Aka2_log4_23	Poz-168166	155	Charcoal	9950 ± 80	11227-11736	11428
Aka2_log5_4	Poz-168168	70	Charcoal	8380 ± 50	9276-9526	9407
AK-P2-36	Poz-182402	400	Charcoal	1400 ±40	1192-1374	1313
Aka2_log5_54	Poz-168167	470	Charcoal	580 ± 50	523-652	597
Aka2_log6_58	Poz-168565	510	Charcoal	8710 ± 80	9534-10117	9702
Aka2_log6_62	Poz-168158	525	Charcoal	9100 ± 310	9535-11141	10260

4.1.2 OSL and pIRIR$_{290}$ dating

348 The equivalent doses for the pIRIR290 multi-grain analyses of AKKA2-OSL1 were computed using the
349 Central Age Model (CAM, Galbraith et al., 1999), giving an OD value of 9 ± 3%, Tab. 2. For the other
350 three sam-ples, the single grain measurements allowed the mini-mum age model (MAM) in order to
351 give more weight to the well-bleached grains and discard saturated grains. The OD value obtained on
352 the SG measurement of AK-KA2-OSL2 is similar to the one obtained on MG ali-quots, of 21%.
353 However, the OD values are higher for AKKA2-OSL3 and 4, of 52% and 61% respectively (Tab. 2).
354 The MAM allowed taking into account the youngest grains, i.e., providing a minimum age estimate for
355 the layer. Ages are displayed in Tab. 2 and range from 82. 9 ± 5.5 ka (AKKA2-OSL1) to 8.5 ± 1.4 ka
356 (OSL3). Note that the yield of accepted quartz grains is low, under 3%. The statistics regarding the single
357 grain selection criteria are available in supplementary material Table. S4. The dose rate data are
358 presented in Tab. 3.

359

360

361

362

363 ***Table 2**;*

364 *Multi-grain (MG) pIRIR290 ages obtained from K-feldspar of sample AKKA2-OSL1 and single-grain (SG) OSL ages obtained from quartz of samples AKKA2-OSL2, 3, and 4*
365 *(1σ uncertainties). For MG analyses, De values were measured on 1 mm diameter aliquots. For SG analyses, quartz grains were mounted on standard 150 µm hole disks,*
366 *reporting accepted (n) and measured (N) grains with overdi-spersion (OD). Alpha and beta dose rates were calculated from radioactive elements (U, Th, K) measured by*
367 *gamma spectrometry (Tab. 3), using conversion factors from Guérin et al. (2011) and alpha attenuation factors (0.14 for U, 0.17 for Th) from Brennan et al. (1991). Gamma*
368 *dose rates were measured in situ (Table 3), and cosmic dose rates were estimated from burial depth (Prescott & Hutton, 1988). Feldspar ages were calculated using the*
369 *Central Age Model (CAM, Galbraith et al., 1999) with beta absorption factors (0.098 for U, 0.139 for Th, and 0.039 for K) as per Guérin et al. (2012) and an α-value of 0.08*
370 *± 25%. The internal dose rate for the K-feldspars was calculated using a K-content assumed of 12 ± 1%. . Quartz ages used the Minimum Age Model (MAM) with beta*
371 *absorption factors (0.100 for U, 0.142 for Th, and 0.041 for K) following Guérin et al. (2012) and an s-a value of 4.5 ± 20%..*

OSL#	**Depth (m)**	**Protocol**	***n*/N**	**De (Gy)**	**OD (%)**	**Dose rate (µGy.a^{-1})**					**Age (ka)**
						Alpha	Beta	Gamma	Cosmic	Total	Age (a)
1	2.25	$pIRIR_{290}$ (MG)	13/15	266 ± 9	9 ± 3	125 ± 22	2019 ± 33	911 ± 22	155 ± 10	3209 ± 45	82.9 ± 5 .5
2	1.2	OSL (SG)	26/1000	135 ± 5	20 ± 5	58 ± 8	2025 ± 16	1074 ± 26	178 ± 10	3335 ± 32	40.5 ± 2. 4
3	2.8	OSL (SG)	17/1000	25 ± 4	52 ± 10	43 ± 6	1757 ± 14	1012 ± 24	144 ± 10	2956 ± 28	8.5± 1.4
4	2.5	OSL (SG)	16/1000	25 ± 2	61 ± 12	42 ± 6	1594 ± 13	837 ± 20	150 ± 10	2622 ± 25	9.500 ± 9

372

Table 3; U, Th and K contents of sediment samples analysed with a laboratory gamma-ray spectrometer equipped with a high-resolution, broad energy Ge (BEGe) detector and in-situ gamma dose rate measured using a portable gamma-ray spectrometer.

OSL#	U (ppm)	Th (ppm)	K (%)	In-situ gamma dose rate (µGy.a^{-1})
1	3.34 ± 0.02	6.56 ± 0.05	1.53 ± 0.01	911 ± 22
2	3.30 ± 0.03	7.60 ± 0.07	2.04 ± 0.02	1074 ± 26
3	2.25 ± 0.02	6.35 ± 0.05	1.89 ± 0.02	1012 ± 24
4	2.27 ± 0.02	5.79 ± 0.05	1.67 ± 0.02	837 ± 20

4.2 Landforms, Textures and Compositions: Multi-Proxy analyses of the alluvial Sequences of Akka

A detailed analysis of the four Akka Plain profiles—based on granulometric, structural, colorimetric, and pedological criteria (including bioturbation intensity, root traces, types and densities of secondary carbonates, and redox features)—identified nine major litho-pedostratigraphic units, further divided into 20 sub-units. These units reflect the local hydrogeomorphological history, encompassing erosion, aggradation, and minor bed mobility.

The lithostratigraphic and chronological results are detailed in section 4.2.1, and the sedimentological and physico-chemical analyses in section 4.2.2. ‘’Multi-proxy analyses and types of pedosedimentary environments’’

4.2.1 Litho-chronostratigraphy

Unit 1 (U1): The basal formation (U1a) is found at the base of both outcrops on the left and right banks (Figure. 3). It consists of a conglomerate deposit made up of heterometric gravels (2–10 cm) set in a greyish sandy matrix (10YR 7/2, light gray), exhibiting a compact texture. The thickness ranges from 40 cm on the left bank to 70 cm on the right bank (Figure.3). No samples were collected from this unit. Above this, Unit 1b (U1b) (Figure. 4a) consists of alternating infill deposits within narrow or flared gravelly channels, which are shallow, along with lenses of heterometric gravels (Figures. 2c and 2d). This sedimentary structure is particularly well-exposed on the right bank, where it displays a braided pattern, indicating high lateral channel migration and significant instability of the floodplain, with a thickness of nearly 2 meters (Figure. 2d). . Overlying this is Unit 1c (U1c), a silty clay deposit (10YR 7/3, very pale brown) with a massive structure containing some secondary carbonate nodules. An OSL date obtained from this formation suggests an age of approximately 82,900 ± 5,500 years.

Unit 2 (U2): This unit, observed only on the right bank of the wadi in profile 4 (fig. 3), consists of a silt deposit approximately 1.50 m thick, (fig.4a) with a greenish-gray color (10YR 7/2, light gray). The deposit exhibits a polyhedral structure and contains some shell fragments. OSL dating places this unit at approximately 40.5 ± 2.4 ka (Table 2).

Unit 3 (U3): This unit is clearly distinguishable in the outcrop by its greenish to light gray color (10YR 7/2, light gray), observed on the left bank of the Akka Wadi (Figures. 2a, 2b, and 3). It appears at the base of profiles 1 and 3 (Figure. 4b) and is characterized by a massive silty facies, 50 to 70 cm thick, containing a few centimeter-sized lenses of heterometric gravels. Above this lies a massive deposit of silt to fine silty sand (U3b), associated with the presence of *Melanopsis* (probably of aff. cariosa type, according to Linnaeus (1789)). This unit (U3), which outcrops discontinuously on the left bank of the Akka Wadi (Figures. 2a, 2b), is preserved over a limited distance of approximately 250 meters to the south. This formation is dated by radiocarbon ^{14}C to around around 11,428 cal BP (11,227–11,736 cal BP).

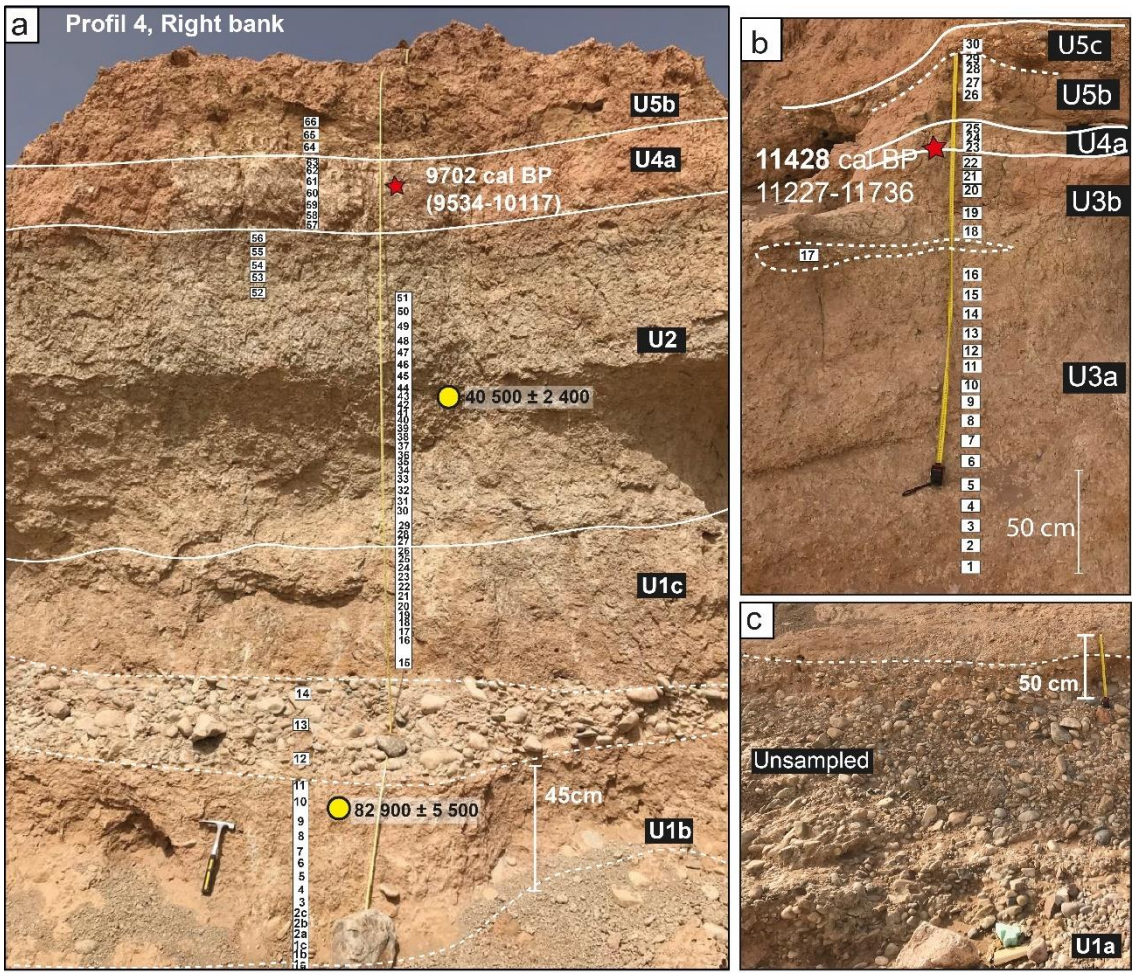

Figure.4. *Field photographs of profiles 3 and 4: a) Sedimentary units of profile 4 on the right bank, showing sample locations and OSL and radiocarbon (^{14}C) dates, b) Profile 3 on the left bank, which forms the base of profile 2, c) Gravelly unit U1a at the base of profile 4.*

Unit 4 (U4): This formation appears at the base of profile 2 (Figure. 5a). It begins with the deposition of a massive clayey silt layer with a pale brown hue (10YR 6/3, pale brown), measuring 50–70 cm in thickness. This basal unit is dated by radiocarbon ^{14}C to approximately 10,520 cal BP (10,097–10,690 cal BP). Overlying this layer is a thicker deposit of brownish clayey silts (U4b) (10YR 5/6, yellowish brown), characterized by intercalated centimeter-scale layers of blackish, highly mineralized peat. The peat is notably flaky and composed of strongly humified plant debris, arranged in indistinct micro-beds (Figure. 5c).

Also present are cylindrical travertine tubes (4–5 cm long, <1.5 cm in diameter) with calcified walls (Figure. 5c), *Melanopsis sp*. shells, and a thin yellowish-orange oxidized lens. Morphologically, this unit represents the sedimentary infill of a broad alluvial channel—approximately 150 meters wide—exposed at the base of profile 2 and extending beneath the modern alluvial plain (Figure. 2a/b/3). The upper part of the unit has been dated to around 9 591 cal BP (9 025–10,187 cal BP).

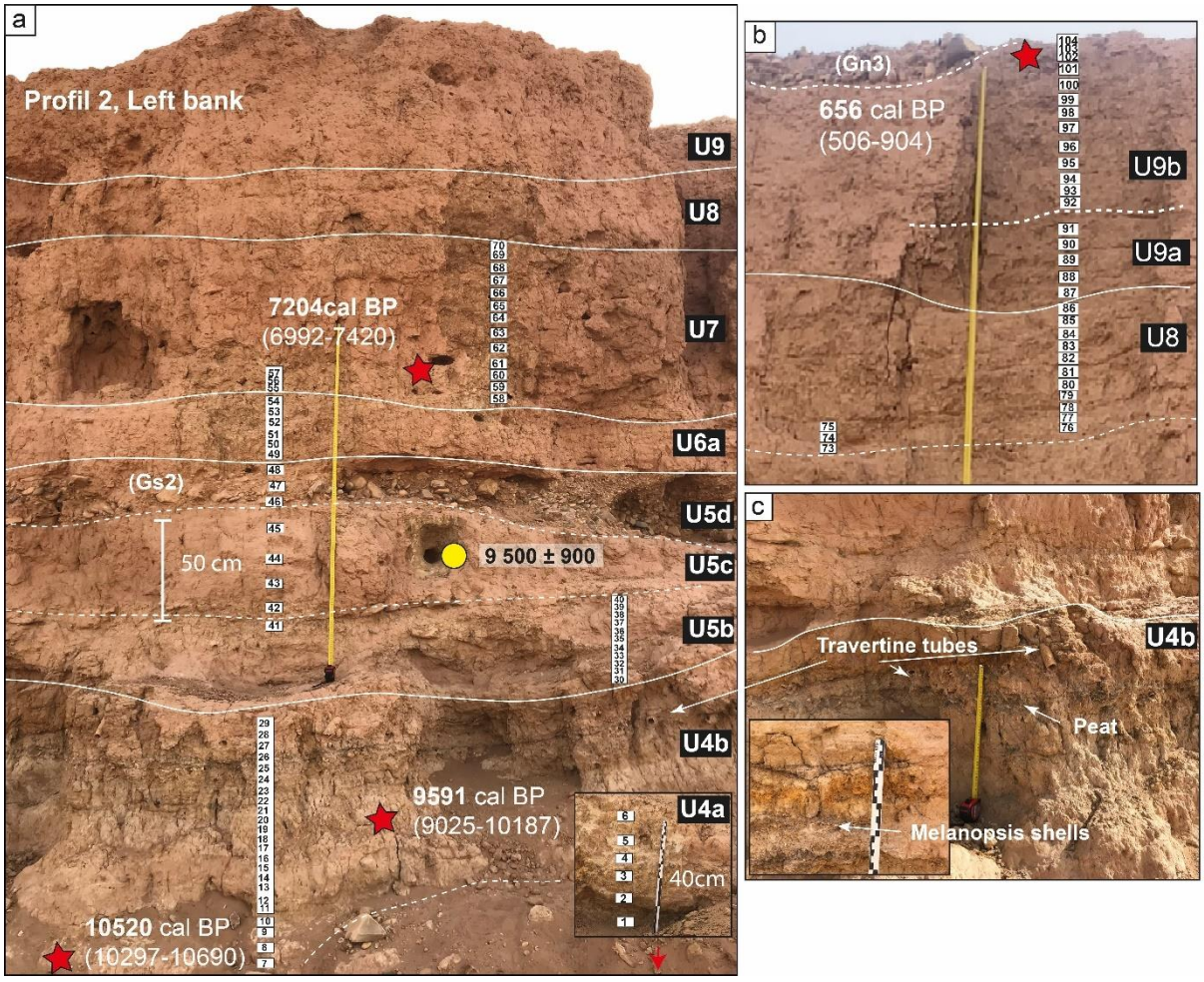

Figure. 5. *Field photographs of profile 2 on the left bank: a) Overview of the sedimentary units composing profile 2, with sample locations and chronological sequence, b) Detailed view of units U8, U9a, and U9b, c) Close-up of unit U3b, highlighting travertine tubes, dark peat layers, and Melanopsis shell fragments.*

Unit 5 (U5) is identified in both the left and right bank deposits of the Akka Wadi (Figure. 3) and comprises four sub-units. Sub-unit U5a is a thin, 10 cm layer of heterometric gravels Gs1 (Gravel sheet) (Figure. 6a), located above U4b. It is discontinuously preserved along the right bank outcrop and marks a lithostratigraphic discontinuity, as it erodes the upper part of the underlying fluvio-palustrine deposits (U4b). This erosional contact indicates a significant shift in sedimentary dynamics, prefiguring the processes that dominate the subsequent sub-units. Sub-unit U5b is composed of massive clayey silts with a light beige color (10YR 6/4 – light yellowish brown), measuring between 40 cm thick on the right bank and up to 1 m on the left bank. This facies includes small tufa lenses forming calcified filaments, as well as shell debris of *Melanopsis sp*. Numerous root traces are also visible, pointing to the development of local hydro-hygrophilous vegetation. Overlying this, sub-unit U5c is a 20 to 60 cm thick layer of homogeneous fine sand of similar coloration (10YR 6/4), marking a transition in sedimentation dynamics and a clear increase in hydrodynamic energy. This intensification culminates in sub-unit U5d, a deposit of heterometric gravels (Gs2) ranging from 10 to 20 cm in thickness, which is consistently visible across the outcrop (Figure. 5a, 6a). This gravel layer reflects a major increase in flow energy, likely associated with a significant incision phase of the wadi between profiles 4 and 3, as illustrated in Figure 3.

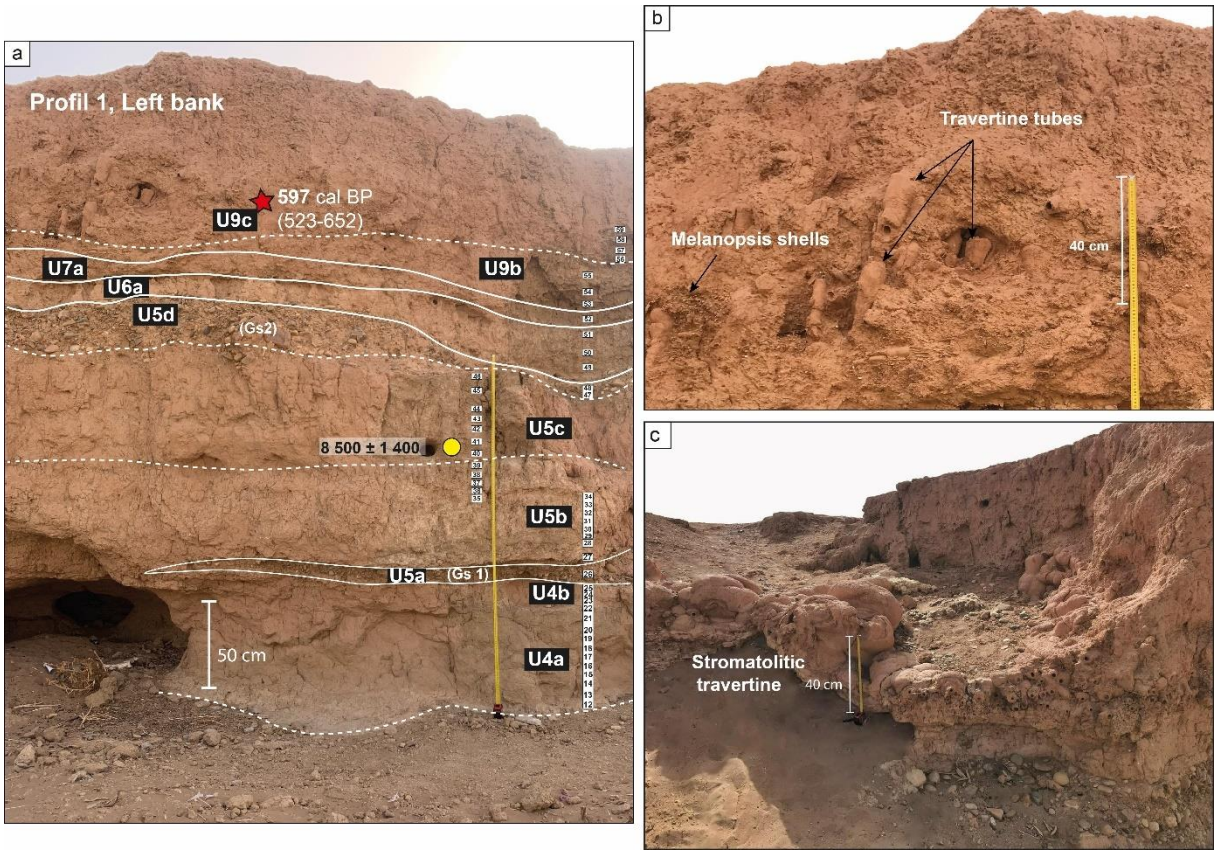

Figure. 6. Field photos of profile 1: a) View of the sedimentary units forming profile 1 on the left bank to the north; b) Zoom on the tuffaceous alluvium deposit (U9c) with large travertine tubes; c) Stromatolithic travertine dam observed to the north of profile 1, deposited at the same level as unit U9c.

Unit 6 (U6) is deposited above the gravelly phase (Gs2) (Figure. 3). It appears in Profiles 1 and 2 (Figures. 5a and 6a) and is characterized by a facies similar to Unit U5b, consisting of massive, tuffaceous clayey silts with a light brown color (10YR 6/4 pale brown). Its thickness ranges from 20 to 30 cm and contains a few *Melanopsis* shells. This formation is dated between 8500 (U5d) and 7204 cal BP (U7a).

Unit 7 (U7) starts with a massive deposit of silt (U7a), light yellowish-brown in color (10YR 6/4), clearly visible in Profiles 1 and 2, with a thickness ranging from 20 to 50 cm. This layer contains a few roots, especially on the right bank in Profile 2 (Figure. 5a). Above it lies a thick layer of silty sand (U7b), varying from 30 cm to 1 m thick in Profile 2. This alluvial plain aggradation features a sometimes well-developed and cemented tufa layer, associated with a few *Melanopsis* shells. The formation is dated to 7204 cal BP (6992–7420 cal BP).

Unit 8 (U8) corresponds to a channel deposit composed of massive silts that overlie Unit U7b (Profile 2) (Figure. 2b), with a thickness of about 50 cm. It extends over 85 meters, exclusively along the left bank in Profile 1 (Figure.2c/d). The unit is also marked by the presence of a few root traces.

Unit 9 (U9) is subdivided into three sub-units, observed in the upper parts of both outcrops on the left and right banks (Figure. 3), south of Profile 4. The first sub-unit, U9a, consists of a loose-textured silty sand deposit with a yellowish-brown color (10YR 5/4) and a thickness of 60 cm (Figure. 5b). The next sub-unit, U9b, is a fine sand layer about 70 cm thick, perforated by numerous root traces. It is overlain by a thin 10 cm layer of heterometric gravels (Gs3), found only in Profile 1 (Figure. 3). This formation is dated to 656 cal BP (506–904 cal BP). The final sub-unit, U9c, is observed only in Profile 1. It comprises a tuffaceous sand layer with a yellowish-brown color (10YR 6/4) and a thickness of 70 cm. This deposit features large, heavily cemented travertine tubes (Figure. 6b), associated with shell fragments.

Unite	S.unite	Color Munsell code	Lithology	Depositional environnemnt	chronology 14C /OSL
U9	9c	10YR 6/4 Light yellowish brown	Alluvial deposit composed of tuffaceous sand Thickness 50 cm Abundance of large travertine lumps associated with shell fragments.	Fluvial stability phase, climatic humidification	
	9b	10YR 5/4 yellowish brown	Massive brownish silty sand. Thickness 55 cm. Covered by a gravel layer (1-2.5 cm). Presence of roots.	High fluvial energy	**579 cal BP (523-652)**
	9a	10YR 5/4 yellowish brown	Homogeneous fine silty sand of dark brown color with a friable texture. Thickness 60 cm.	Increase in fluvial energy	**656 cal BP (506-904)**
U8	8a	10YR 5/4 Yellowish brown	Brownish silt with a massive structure. Thickness 50-80 cm. Presence of a few roots.	Low hydrodynamics favors the formation of vegetation	
U7	7b	10YR 6/4 Light yellowish brow	Silty tuffaceous sand of brownish color, massive. Thickness 30 cm - 1 m. Presence of a few shell fragments and roots.	Variation in flow energy with a calm and humid paleoenvironment	**7402** cal BP (6992-7420)
	7a	10YR 6/4 Light yellowish brown	Tuffaceous silts of brownish color. Thickness 20-50 cm. Presence of a few root traces.	Low hydrodynamics favors the formation of vegetation	
U6	6a	10YR 6/3 Pale brown	Clayey silts with layers of tuff, brownish in color, massive. Thickness 20-30 cm. Presence of a few Melanopsis shells.	Low hydrodynamics, showing a variation in flow energy. Return to humid conditions.	
U5	5d	10YR 6/4 Light yellowish brown	Heterometric pebbles (2-7 cm) embedded in a grayish sandy matrix. Thickness 10-20 cm.	Strong hydrodynamics of the environment, flood phase, sedimentation disruption	
	5c	10YR 6/4 Light yellowish brown	Homogeneous fine sand of brownish color. Thickness: 20-60 cm. Presence of a few roots.	Transition deposit showing a change in hydrodynamics of the environment,	**8 500 ± 1 400** **9 500 ± 900**
	5b	10YR 6/4 Light yellowish brown	Massive light brown clayey silts. Thickness: 40cm to 1m. Composed of alternating layers of fine silty sand, with the presence of roots and a few Melanopsis.	Low hydrodynamics deposit, with a variation in fluvial energy	
	5a	10YR 5/6 Yellowish brown	Heterometric gravel layer with a thickness of 10 cm.	Flood period with a sudden increase in fluvial energy	
U4	4b	10YR 5/6 Yellowish brown	Massive brownish clayey silt, 1 m in thickness. Characterized by an alternation of centimeter-thick layers of dark peat, associated with Melanopsis shells and travertine tubes, with roots. A thin layer of yellowish silt indicates oxidation	Low-energy fluvial deposit showing weak hydrodynamics, forming a sedimentation deposit (fluvio-lacustrine environment)	**9591** cal BP (9025-10187)
	4a	10YR 6/3 Pale brown	Beige silty clay, with chanel deposit, composed of fine sand to fine silty sand, laminated, brownish in color, 20- 80 cm in thickness. Presence of carbonate nodules with some roots.	Low-energy fluvial deposit showing weak hydrodynamics (fluvio-lacustrine environment)	**10520** cal BP (10297-10690) **9702** cal BP (9534-10117)
U3	3b	10YR 7/3 very pale brown	Massive silty sand, greenish in color, 30-50 cm in thickness+ Melanopsis shells	Aggradation deposit, with low fluvial energy	**10260** cal BP (9235-11141)
	3a	10YR 7/2 Light gray	Fine greenish silt with a massive structure, 50-70 cm in thickness. Millimetric lenses of coarse sand-gravel. Presence of some Melanopsis shells		**11428** cal BP (11227-11736)
U2	2a	10YR 7/2 Light gray	Greenish silt with a polyhedral structure, 2 meters thick. Presence of some Melanopsis shells.	Aggradation deposit, with low fluvial energy	**40 500 ± 2 400**
U1	1c	10YR 7/3 very pale brown	Greenish clayey silt, 50 cm in thickness. Massive structure with carbonate nodules.	Transition deposit, showing a decrease in fluvial energy with a rise in groundwater level	
	1b	10YR 6/4 Light yellowish brown	Brownish silt, 1.50 m in thickness. Alternating deposits of narrow and shallow channels, composed of heterometric gravel (sorting facies)	Strong lateral mobility of the floodplain	**82 900 ± 5 500**
	1a	10YR 7/2 Light gray	Heterometric pebbles and gravel (2-10 cm) of grayish color embedded in a sandy cement, 40-70 cm in thickness	Strong hydrodynamics with relatively fast deposition conditions. Arid paleoenvironment	

***Table 4**: synthetic description of the lithostratigraphic facies and the deposits related to the sedimentary environments identified in the Akka sequences*

4.2.2 Multi-proxy analyses and discussion of sedimentary environment types

The cross-analysis of sedimentological and physico-chemical data (Figure. 7) allows for the reconstruction of past environmental dynamics of the Akka plain. Based on the results obtained, three

main types of pedosedimentary environments (TPE) have been identified. Each of these environments is characterized by specific features reflecting depositional conditions (grain size, hydrodynamic energy), the degree of pedogenetic alteration, carbonate precipitation dynamics, organic matter accumulation, redox conditions, and sediment provenance. These elements are summarized in Table 5.

These parameters were assessed using a series of environmental proxies : Grain size indices (D50 and D90) indicate depositional energy; Magnetic susceptibility (MS) and the Rb/Sr ratio inform on the intensity of pedogenetic processes, sometimes associated with high concentrations of organic matter; Carbonate content ($CaCO_3$) and the Ca/Mg ratio reflect carbonate precipitation conditions, organic matter (OM) content indicates biological productivity or the preservation of authigenic vegetation, the Fe/Mn ratio is used as a marker of redox conditions, finally, the Si/Al ratio serves as an indicator of detrital input and can also be interpreted as a proxy for aridity.

- **TPE 1 : Low-energy fluvio-palustrine environment**

This type of environment includes units U1b, U2, U3a, and U4b (Figure. 7). It is characterized by a high proportion of fine particles (silt and clay), representing between 70% and 90% of the total grain size, with a clear dominance of silt. D50 and D90 values below 30 µm indicate very calm depositional conditions, typical of stable, shallow, or even semi-permanent settings such as wetlands or marshes. Magnetic susceptibility is low (5 to 10 × 10^{-8} $m^3 \cdot kg^{-1}$), consistent with a low concentration of magnetic allogenic minerals, often linked to organic or carbonate-rich environments. The Rb/Sr ratio is generally high, indicating significant pedogenetic alteration, possibly due to leaching processes or in-situ soil formation. Carbonate contents ($CaCO_3$) are high (50–65%), as are Ca/Mg ratios, suggesting carbonate precipitation under calm conditions, favored by bicarbonate-rich groundwater inputs. These deposits may be associated with the formation of carbonate tufas, particularly in the presence of dense vegetation and good water retention. Organic matter is abundant (20–50%), reflecting either local high biological productivity or/and good preservation under hydromorphic conditions. The Fe/Mn ratio shows medium to high values, indicating alternations between oxidizing and reducing conditions, common in periodically saturated environments. Lastly, the Si/Al ratio is generally low, suggesting limited detrital input and supporting the hypothesis of a closed environment with minimal allochthonous influence.

Overall, these features indicate a low-energy fluvio-palustrine environment, with high biological production, carbonate precipitation, organic soil development, and frequent hydromorphic conditions—typically associated with wetter climatic phases or/and high groundwater levels.

- **TPE 2 : Low-energy (carbonate-rich) floodplain**

This environment includes units U3b, U4a, U6, and U9c (Figure. 7). The grain size distribution is dominated by silty fractions (60–80%), with D50 values below 50 µm, indicating low to moderate depositional energy. Magnetic susceptibility (MS) ranges from 5 to 15 × 10^{-8} $m^3 \cdot kg^{-1}$, indicating a moderate presence of magnetic minerals. The Rb/Sr ratio is variable. Carbonate contents ($CaCO_3$) are moderate to high (50–70%), with high Ca/Mg ratios, suggesting carbonate precipitation partially linked to biogenic processes or calcium-rich groundwater inputs. Organic matter (OM) is moderately abundant, generally between 10% and 30%. Redox conditions are variable, with occasional Fe/Mn peaks, indicating a frequently water-saturated environment with possible fluctuations. The Si/Al ratio is generally low, indicating limited detrital input. However, some units (notably U5b, U6a, U7a, and U8) show peaks in the Si/Al ratio, indicating changes in sediment sources after 9700 cal BP, reflecting an increase in fluvial detrital or aeolian influence. Altogether, these indicators reflect a calm and humid floodplain environment with fine sediment deposits, moderate to advanced pedogenesis, and carbonate precipitation. This type of setting corresponds to sub-humid to humid climatic conditions, with shallow groundwater tables and diffuse runoff and floods events.

It is characteristic of low-energy floodplains, where water is present temporarily or semi-permanently, favoring the deposition of fine and relatively stable sediments. These environments are often associated with channel margins, overflow areas, or wetlands fed by groundwater or diffuse surface flow.

- **TPE 3 : Dynamic high-energy alluvial environment**

This environment includes units U1a, U5a, U5c, U5d, U7, U9a, and U9b (Figure. 7). The grain size is coarse, dominated by sand (70–80%) and sometimes gravel, indicating high hydrodynamic energy and stronger connectivity with upstream areas. Grain size indices are high (D50 > 100 µm, D90 > 220 µm), and the Zr/Rb ratio is also significant, confirming rapid and energetic fluvial transport. Magnetic susceptibility varies (10 to 50 × 10^{-8} $m^3 \cdot kg^{-1}$), with high values in certain units (e.g., U5a, U9b), indicating a stronger contribution of detrital magnetic minerals. The Rb/Sr ratio is low, reflecting limited mineral alteration due to rapid deposition and minimal pedogenetic development. Carbonate contents ($CaCO_3$) are moderate (40–50%), with low Ca/Mg ratios, indicating a context where carbonate precipitation is not favored due to the high-energy depositional dynamics. Organic matter content is very low (2–15%), reflecting a very detrital environment unfavorable for its accumulation and frequently subject to remobilization. The Fe/Mn ratio is highly variable, suggesting possible alternations between oxidizing and reducing phases.

Finally, the Si/Al ratio is high, confirming a substantial input of coarse detrital material of aeolian or torrential origin.

Overall, this type of environment reflects an active, high-energy alluvial setting dominated by coarse inputs, minimal soil development, poor organic matter preservation, and indicative of episodic flood phases, aeolian redeposition of alluvial deposits associated to drier climatic conditions.

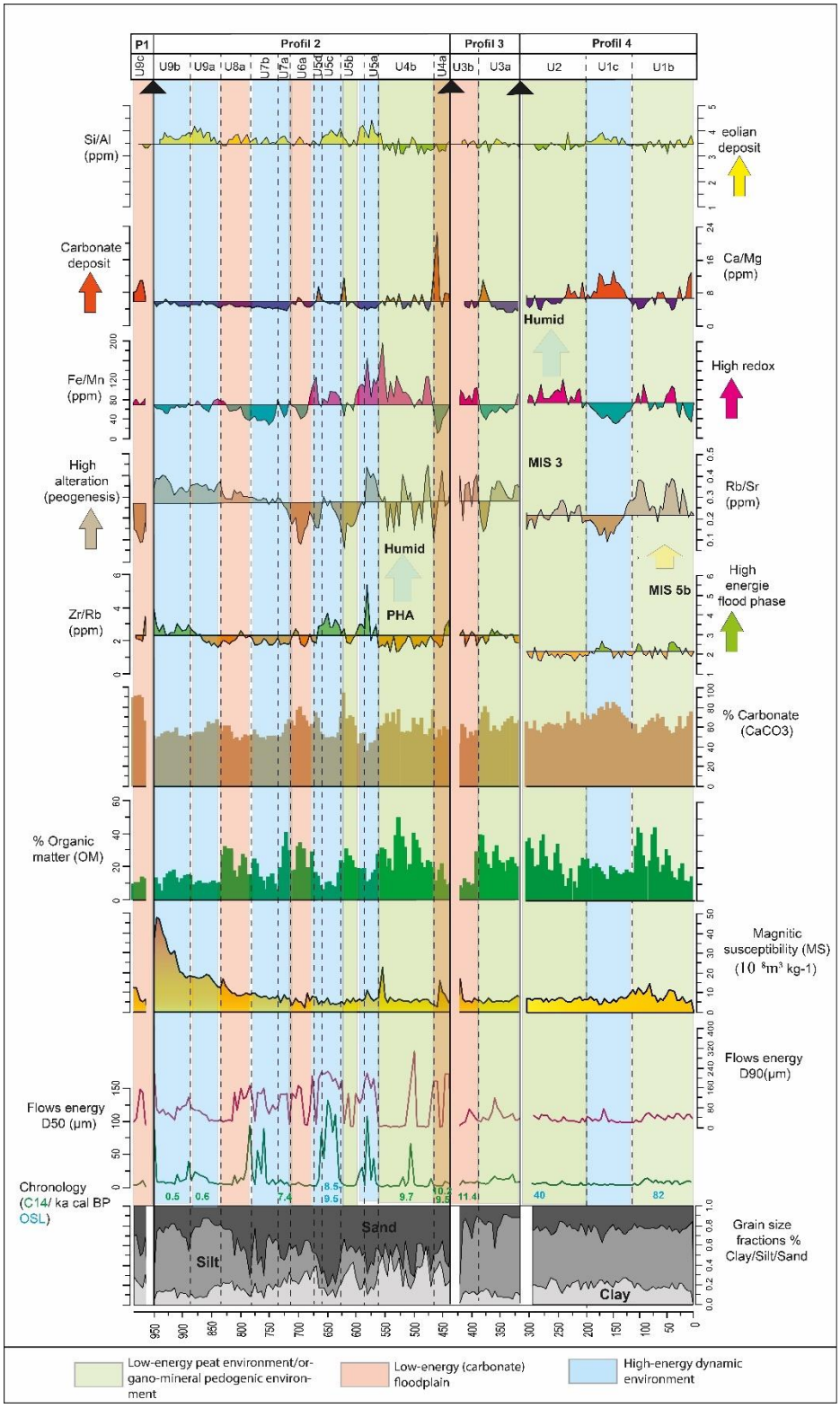

548 ***Figure. 7.*** *Correlation diagramms of the principal granulometric, magnetic, and geochemical properties from*
549 *the four studied profiles, integrated to propose a reference cross-section of the Akka alluvial sequence. Colored*
550 *bands highlight the distinctive characteristics of each sedimentary unit. Geochemical ratios are expressed*
551 *relative to the average values of each ratio. Black arrows atop the curves indicate sedimentary discontinuities*
552 *within the alluvial record.*

553 *Table 5: Comparative summary of Pedosedimentary Environment Types (TPE).*

Characteristics	**TPE 1: Low-energy fluvio-palustrine**	**TPE 2: Low-energy floodplain (carbonate-rich)**	**TPE 3: High-energy dynamic environment**
Units	U1b, U2, U3a, U4b	U3b, U4a, U6, U9c	U1a, U5a, U5c, U5d, U7, U9a, U9b
Dominant grain size	Fine particles (silt + clay): 70–90%	Dominantly silt: 60–80%	Sand and gravel: 70–80%
D50 / D90	Very low: < 30 µm	Low: < 50 µm	High: D50 > 100 µm; D90 > 220 µm
Hydrodynamic energy	Very low (stable or stagnant environment)	Low (calm and moist environment)	High (floodplain or active channel)
Magnetic susceptibility (MS)	Low: 5–10 $\times 10^{-8}$ m³/kg	Moderate: 5–15 $\times 10^{-8}$ m³/kg	Variable: 10–50 $\times 10^{-8}$ m³/kg
Rb/Sr ratio (pedogenesis/versus soil erosion)	High (intense weathering)	Variable	Low (limited weathering)
Carbonates ($CaCO_3$, Ca/Mg ratio)	High $CaCO_3$ (50–65%); high to moderate Ca/Mg	High $CaCO_3$ (50–70%); variable Ca/Mg	Low $CaCO_3$ (40–50%); low Ca/Mg
Organic matter (OM)	Abundant: 20–50%	Moderate: 10–30%	Low : 2–15%
Fe/Mn ratio (redox conditions)	Variable to high (alternating oxidation/reduction)	Variable (sporadic peaks)	Variable (possible alternation)
Si/Al ratio (detrital-aeolian input)	Low (limited input, enclosed environment)	Low to moderate (sporadic peaks after 9700 BP)	High
Environmental context	Palustrine or peat-forming environment, low energy, high water table	Calm floodplain, shallow water table	Active alluvial environment, floods, high dynamics, aeolian redistribution in floodplain
Climatic significance	Humid climates, stagnation, dense vegetation	Sub-humid to humid climate, diffuse runoff	Drier climates or periods of intense episodic flooding

554

4.3 Principal Component Analysis (PCA)

In order to gain a better understanding and simplify the analysis of the geochemical dataset obtained from X-ray fluorescence (XRF), we conducted a Principal Component Analysis (PCA). For a clearer representation of the results, only the most representative units from each profile were selected, thus forming the core geochemical dataset (Figure 11 in supplementary material)

Figure 8 shows the PCA biplot, where two axes are represented. Axis Dim1 explains 32% of the total variance, and axis Dim2 accounts for 20.7%, giving a cumulative total of 52.7% of the overall inertia. The colored dots represent the samples, coded according to depth, with a gradient ranging from blue at the base of the sequence to orange at the top. The black arrows represent the geochemical variables, with their direction indicating correlation with the axes, and their length reflecting the strength of that correlation. The samples cluster into units (U1b, U2, U4b, U7b, U8, U9, and U5c), highlighting their relationships with certain elemental variables.

The first dimension (Dim1), which explains 32% of the total variance, contrasts two groups. On the left side, there is a positive correlation between calcium (Ca), sulfur (S), and manganese (Mn) with the samples from units U1b and U2. Calcium and sulfur reflect carbonate and evaporite deposits. Their joint enrichment suggests carbonate deposits associated with hydrological fluctuations of the water table. On the opposite side, to the right, titanium (Ti), potassium (K), aluminum (Al), and magnesium (Mg) show a positive correlation with the samples from units U7b and U8. Titanium, of continental origin, is mainly linked to coarse detrital inputs, while potassium and aluminum, associated with clay minerals, reflect finer sediment inputs. This elemental grouping characterizes an alluvial minerogenic detrital dynamic.

The second dimension (Dim2), which accounts for 20.7% of the variance, separates two trends. In the upper part, iron (Fe) and rubidium (Rb) show a positive correlation with units U1b, U2, and U4b. Iron, a terrigenous element frequently used as a redox indicator (Rothwell & Croudace, 2015), reflects variations in the oxidation conditions of the environment but also is involved in pedogenesis processes, while rubidium, generally associated with fine clay deposits, indicates detrital input in a low-energy context, potentially linked to pedogenetic or soil erosion processes. In the lower part, zirconium (Zr) and silica (Si) are enriched in the samples from units U9a, U9b, and U5c. These elements, contained in resistant minerals to physical and mechanical processes such as zircon, reflect high-energy deposits and suggest a predominantly aeolian and/or torrential river inputs.

Overall, this analysis allows for the distinction of three main sedimentary poles: carbonate deposits with redox conditions represented by units U1b, U2, and U4b; alluvial detrital inputs mainly grouping units

U7b and U8; and finally, coarse deposits with a dominant aeolian origin characterizing units U9a, U9b, and U5c.

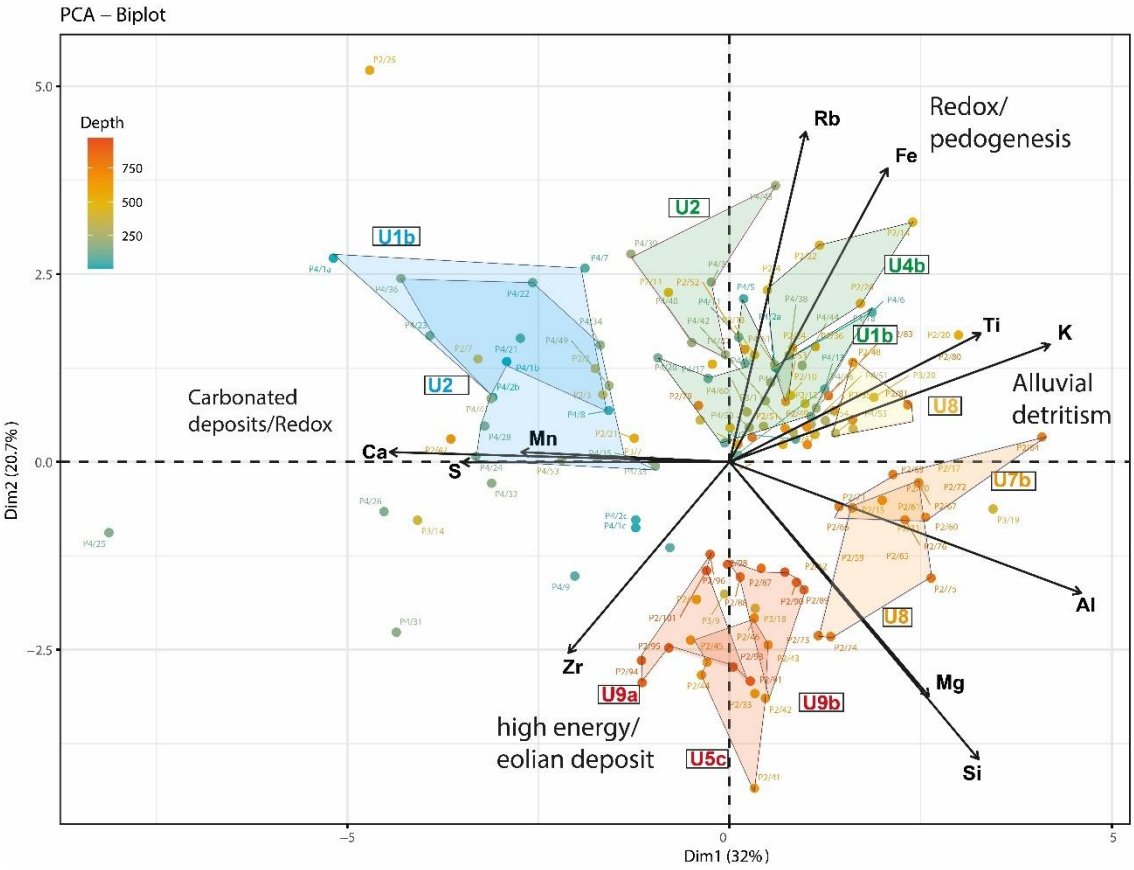

Figure. 8. *Results of the Principal Component Analysis (PCA) performed on the Akka geochemical dataset. Colored areas associated with clusters of projected samples emphasize the hydro-sedimentary and environmental contexts corresponding to each correlation group.*

5. Synthesis and Discussion: morphosedimentary and paleoenvironmental evolution of the Akka Plain in relation to climatic variations from the last glacial Period to the Holocene at local, regional, and supraregional scales

In this section, we discuss the morphosedimentary and paleoenvironmental evolution of the Akka Plain. Our analysis draws on the geochemical composition and sedimentary dynamics of the formations, alongside the concurrent development of the alluvial plain's geomorphological setting and the chronological framework of the deposits. By correlating these proxies, we reconstruct the local geomorphological and paleoenvironmental history of the plain from the Late Pleistocene (MIS 5b) to the present (Figure 9).. These results are compared with similar reconstructions from alluvial archives across North Africa, as well as with recently published paleoenvironmental and paleoclimatic data at local, regional, and supraregional scales throughout the eastern Sahara and North Africa (Figure 10). Our approach involves correlating evolutionary histories reconstructed in other regions to validate and

strengthen our local findings, thereby situating them within the broader context of paleoenvironmental dynamics.

5.1 MIS 5b (ca. 82.9 ± 5.5 ka): Fluvial Aggradation and Hydroclimatic Instabilities

During Phase 1, dated to approximately 82.9 ± 5.5 ka, the Akka plain records a marked phase of aggradation, characterized by sediment accumulation reaching up to 4.5 meters in thickness. The sedimentary sequence displays a fining-upward trend: coarse sediments at the base gradually give way to finer materials, interspersed with gravelly layers in the upper section. These deposits are associated with narrow and shallow channels, where massive, heterometric gravel unit are observed—typical of a braided river system. This type of fluvial dynamic is generally seen in deep valleys subjected to highly variable hydrological regimes or in response to exceptional rainfall events (Lghamour et al., 2024) Paine et al., (2024).

The silty matrix binding the gravel elements suggests deposition during waning flood stages. It also indicates the probable presence of permanent ponds during low-flow periods. These features reflect strong alluvial activity driven by unstable hydroclimatic conditions, likely linked to the end of the last interglacial period (Marine Isotope Stage 5), a phase still poorly documented in the fluvial archives of southern Morocco and Northern Africa.

This interpretation is supported by data from the Wintimdouine cave stalagmite, located about 200 km west of Akka and 30 km north of Agadir (Brahim et al., 2017; Brahim et al., 2023). Isotopic analysis of this karst archive reveals a period of high rainfall between 84 and 77 ka BP, during the Late Pleistocene, reflecting intensified precipitation and regional runoff. The variability of $\delta^{13}C$ and $\delta^{18}O$, with more negative values around 80 ka and more positive values near 73 ka, suggests that both proxies respond to the same orbital-scale climatic forcing (Brahim et al., 2023).

Meanwhile, records from Dim Cave in southern Turkey show a peak in detrital input during the MIS 5a–MIS 4 transition (81–70 ka), associated with increased erosion, surface weathering, and progressive mineralogical changes (Paine et al., 2024). These developments indicate a decline in regional moisture availability, followed by a pronounced aridity peak after 74 ka, corresponding to a rapid transition to intense cold and dry conditions observed across the Northern Hemisphere's paleoclimatic archives.

5.2 MIS 3 (ca. 60–30 ka): Evidence of fluvial dynamics and relationship to humid/arid fluctuations

Around 40,500 ± 2,400 years ago, during Marine Isotope Stage 3 (MIS 3), the Akka plain experienced a new phase of aggradation (Figure 9), represented by the silty unit U2. This unit, about 1 meter thick, is characterized by predominantly fine deposits (over 80% silt), indicating a stable sedimentary environment influenced by low-energy hydrological dynamics. The greenish-grey color (10YR 7/2), the

massive polyhedral structure of the deposit, and a high organic matter content (over 30%) confirm the presence of active hydromorphic pedogenetic processes associated with a high, quasi-permanent fluvial aquifer, during sedimentation. These features point to a prolonged period of soil exposure, consistent with a phase of relative landscape stability.

The sedimentological characteristics, confirmed by associated grain-size and geochemical analyses, suggest a low-energy depositional environment with limited aridity, supporting the hypothesis of a more humid climate during this period.

Available paleoenvironmental and paleoclimatic data on MIS 3 in Morocco, although limited, reinforce these observations. In the southern part of the country, geomorphological analyses of the fluvial systems of the wadi Tamadroust and Wadi Noun reveal the accumulation of lacustrine deposits dating between 50 and 30 ka BP. These findings indicate low-energy fluvial activity during MIS 3, in a relatively humid climatic context (Weisrock et al., 2006). At the regional scale, alluvial archives from the Falémé Valley in Senegal also document a high load of fine sediments and progressive aggradation of the riverbed during MIS 3 and 2 (Rasse et al., 2020) (Figure 10). These observations are further supported by the work of Preusser et al. (2002), who reported an absence of aeolian remobilization in the Wahiba Sands region of Oman (Eastern Arabia) between 64 and 22 ka BP, indicating a prolonged humid phase between 58 and 32 ka BP.

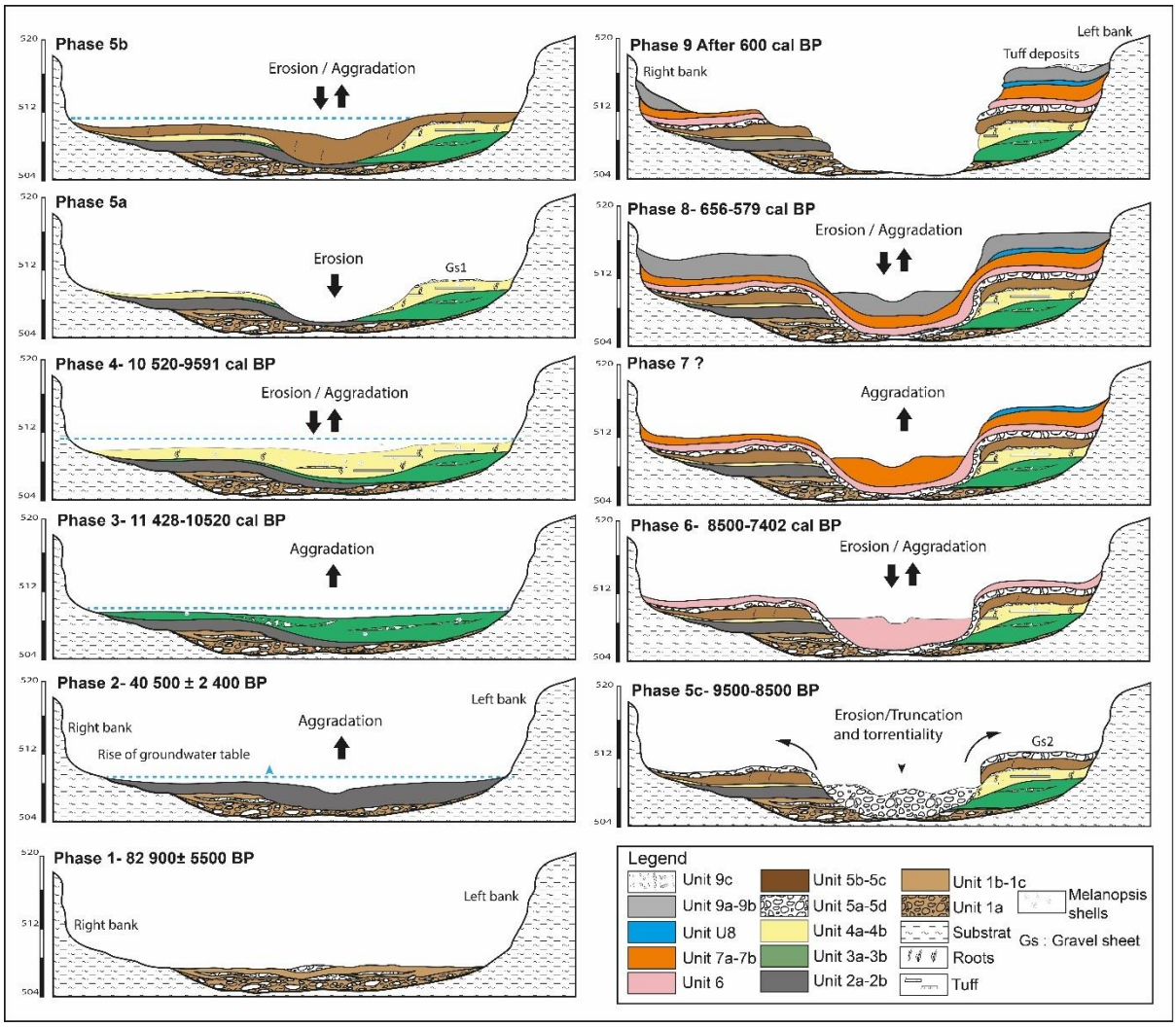

Figure. 9. *Model of the geomorphological and paleoenvironmental evolution of the Akka plain to since MIS 5b, Phases 5a, 5b and 7 present an imprecise chronology due to the lack of carbonaceous material within the sedimentary units*

5.3 Late Pleistocene / Younger Dryas (15–11.5 ka): fluvial reactivation and early signs of the African Humid Period

This phase (Figure 9), dated between 11,428 and 10,520 cal BP, begins with a clear incision of the riverbed on the left bank, followed by fine alluvial aggradation forming unit U3, with a thickness ranging from 1.5 to 2 meters. This sequence reflects fluctuating hydrological dynamics: at its base, the deposits indicate a low-energy fluvio-palustrine environment, which gradually transitions to conditions still dominated by low energy but intermittently disrupted by brief, more powerful hydrological events, as evidenced by the localized presence of coarse sand layers interpreted as the result of sudden flood events.

Similar dynamics have been documented further north, in Morocco particularly in the sedimentary records of the Noun, Assaka, and Kert rivers, as well as in the Moulouya Basin, where indicators of hydrological reactivation and hydromorphy appear between 11,500 and 10,800 cal BP (Ouammou,

669 1993; Boudad et al., 2003; Mathieu et al., 2004; Zielhofer et al., 2008). Despite the limited dating of
670 alluvial archives in some areas of southern Morocco, such as thocse from the Wadi Noun (Weisrock et
671 al., 1991), and the scarcity of data from Saharan fluvial systems in this region, the deposits from the
672 Akka plain represent the first clear and well-dated evidence of hydrological dynamics associated with
673 the African Humid Period (AHP) in southern Morocco.

674 **5.4 Early Holocene / African Humid Period 11.5–8 ka BP**

675 This phase, dated between 10,520 and 9,591 cal BP, begins with a marked incision of about 1.5 m,
676 cutting into the previous phase as well as the underlying Pleistocene formations (Figure 9). It is followed
677 by a fine alluvial aggradation reaching a thickness of 2 m, represented by unit U4. This phase is part of
678 the Early Holocene dynamics, characterized by a progressive intensification of regional humidity,
679 corresponding to the first manifestations of the last African Humid Period (AHP).

680 The sedimentological and geochemical characteristics of this sequence indicate a low-energy fluvial
681 system, favorable to the development of stable marshy environments. The abundance of authigenic
682 organic matter deposits (peat), the accumulation of carbonates (tufa), and the high silt content point to
683 persistently humid climatic conditions, under the effect of increased and more evenly distributed rainfall
684 throughout the year. This hydrological context promoted the expansion of wetlands in valley bottoms,
685 the formation of organic-rich soils associated with hygro-hydrophilous vegetation, and the presence of
686 weakly active alluvial channels.

687 The localized presence of *Melanopsis shells* associated with tubular tufa deposits (Figure 5c) indicates
688 slow and perennial flow in a freshwater environment saturated with calcium bicarbonate. This
689 interpretation is supported by several geochemical indicators (Figure 7) pointing to very low-energy
690 conditions in a hydromorphic environment with high water stability. The observed oxidation deposit
691 shows a subsequent partial drying of the channel bed.

692 At the regional scale, comparable sequences have been identified in the alluvial archives of the wadi
693 Noun, characterized by fluvio-lacustrine deposits rich in organic matter, stagnant waters, and evidence
694 of pedogenesis (Weisrock, 1980; Chennaoui et al., 2005; A. Weisrock et al., 2006). In the Moulouya
695 basin, sedimentary and palynological data reveal the presence of marshy environments and carbonate
696 tufa formation between 10,800 and 9 000 cal BP, associated with strong hydrological stability (Depreux
697 et al., 2021). These environments reflect prolonged humid conditions, confirmed by the identification
698 of several successive palynological biozones, the oldest indicating the presence of shallow lakes before
699 10,600 cal BP, followed by a marked aridification episode around 5 000 cal BP (Limondin-Lozouet et
700 al., 2013).

Beyond the Moroccan context, Early Holocene humid sequences are well documented at the North African scale. In the Niyes peat bogs, Senegal (Figure 10), archives reveal a more wooded landscape, a high water table, and a strengthening of the monsoon around 9500 cal BP (Ndiaye et al., 2022). Data from Lake Chad also show a rise in lake level between 9500 and 6500 cal BP, characterized by low $\delta^{18}O$ values and low conductivity, pointing to a positive water balance. In the Tadrart Acacus massif, southern Libya, the reactivation of springs is attested by travertine deposits dated to around 9500 cal BP (Figure 10j), associated with a renewed activity of large Saharan hydrological systems (Cremaschi et al., 2010; Cremaschi & Zerboni, 2011). Further indications of the African Humid Period are found in Saharan paleo-lakes such as Hassi el Mejnah and Sebkha Mellala in Tunisia, which show an abrupt transition from arid to lacustrine conditions around 10,500 cal BP. These data collectively mark a hydrological optimum, particularly in high-latitude regions (Fontes et al., 1985; Gasse et al., 1990; Gasse, 2002).

These records reflect increased regional and supra-regional humidity, driven by enhanced precipitation resulting from intensified summer insolation around 12 ka cal BP (Berger & Loutre, 1991). This insolation peak caused a northward migration of the Intertropical Convergence Zone (ITCZ), which shifted approximately 500 to 800 km beyond its current position (Petit-Maire et al., 1995 ; Gasse, 2000; Maley & Vernet, 2013). This shift facilitated the expansion of the West African monsoon domain, triggering significant climatic transformations across the region. The resulting increase in precipitation not only reactivated fluvial systems but also induced substantial changes in local ecosystems, promoting the development of wetter and more wooded landscapes (Kutzbach, 1981; DeMenocal & Tierney, 2012; Pausata et al., 2020). It is also noteworthy that the deserts of the Arabian Peninsula experienced a contemporaneous humid phase during the early to mid-Holocene, coinciding with these African climatic shifts (Yan & Petit-Maire, 1994; Lézine et al., 1998; Fleitmann et al., 2007). This synchronicity suggests that these climatic changes had a broad geographic reach, affecting not only the Sahara but also other arid regions at similar latitudes.

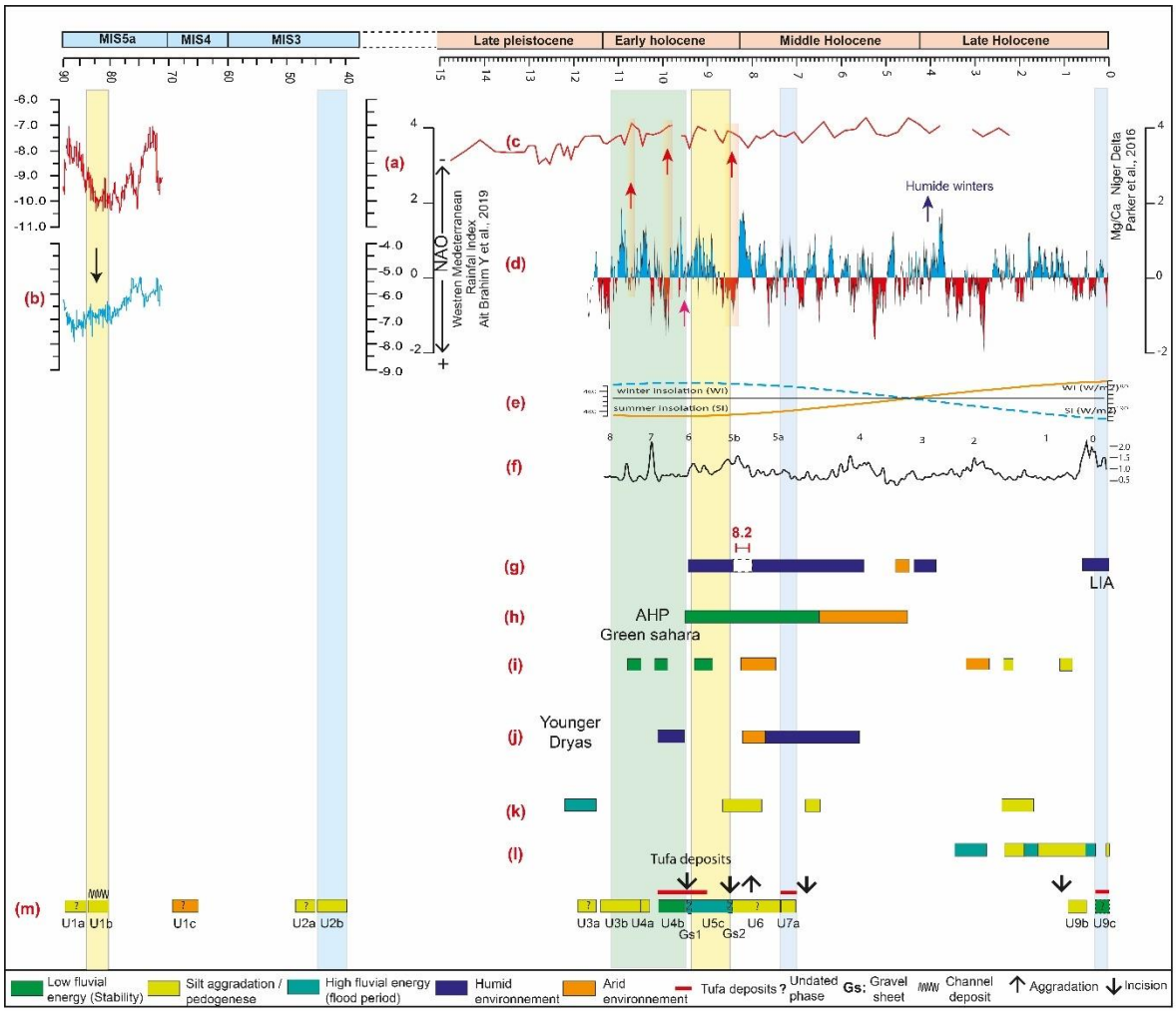

Figure. 10. Comparison of environmental and climatic records during the Late Pleistocene (MIS 5b) and the Holocene in North Africa. Chronology is expressed in calibrated years before present (cal BP). Blue bands represent humid periods, while yellow bands indicate arid environmental phases. a) Paleoclimatic $\delta^{13}C$ record from speleothems in Wintimdouine (Brahim et al. 2023) , b) Paleoclimatic $\delta^{18}O$ record from speleothems in Wintimdouine (Brahim et al., 2023) , c) Mg/Ca ratio curve as a sea surface temperature (SST) proxy from planktonic foraminifera shells (Globigerinoides ruber) (Parker et al., 2016), d) Precipitation index for the western Mediterranean basin derived from speleothems from Chaara cave (Ait Brahim et al., 2019), e) Summer and winter insolation curves at 40°N (A. Berger & Loutre, 1991), f) North Atlantic ice-rafted debris records showing both tuned and original datasets, with numbered Bond events chronology (Bond et al., 2001), g) Paleoenvironmental records from the Niayes peat bog, northern Senegal (Ndiaye et al., 2022), h) Climatic reconstructions from fossil diatoms in paleolakes in central Sahara, Chad (Yacoub et al., 2023), i) Paleoenvironmental records from the Charef River, northern Morocco (Depreux et al., 2022; Depreux et al., 2021), j) Environmental records from the Takarkori River, southwestern Libya (Cremaschi et al., 2014), k) Environmental records from the Yami River, Sahara, western Africa (Lespez et al., 2011), l) Holocene paleoenvironmental record from the middle Drâa basin (Saadi et al., 2024), m) Paleoenvironmental archives from the Akka plain (this study). Question marks in the Akka sequence highlight phases with chronological uncertainty.

5.5 Middle and Late Holocene (after 8 000 cal BP)

The Middle and Late Holocene mark a notable change in the morpho-sedimentary, hydrodynamic, and paleoenvironmental dynamics of the Akka plain. This period is characterized by the appearance of numerous truncations and hiatuses, suggesting a transition to more arid conditions, accompanied by high

747 fluvial energy. Three distinct phases are identified in the Akka plain during this period: phase 5,
748 subdivided into three sub-phases (5a, 5b, and 5c), as well as phases 6 and 7. These different phases
749 illustrate a marked variability in fluvial dynamics and climatic conditions, typical of the Middle
750 Holocene (Renssen et al., 2003; Roberts et al., 2011; Fletcher et al., 2013; Berger et al., 2016)

751 - Phase 5a: Fluvial incision and erosive dynamics

752 The first sub-phase, corresponding to unit U5a, is marked by significant fluvial incision (Figure 9),
753 estimated between 1 and 1.5 meters deep, cutting into the alluvium of the previous phase. Grain-
754 size and geochemical analyses reveal a notable increase in flow energy, characterized by a high
755 proportion of coarse fractions and elevated Zr/Rb and Si/Al ratios. These markers indicate an
756 episode of intense erosion, resulting in a negative sedimentary record (erosive truncation), probably
757 linked to episodic alluvial discharges and significant aeolian input. This abrupt change reflects a
758 substantial drop in the alluvial water table and hydrological instability in the Akka plain. This event
759 could be associated with a regional arid phase that occurred around 9 300 cal BP, linked to the global
760 Rapid Climate Change (RCC) event of that period. Similar dynamics have been observed in the
761 Moulouya basin, where a nearly synchronous depositional hiatus has been identified (Depreux et
762 al., 2022).

763 - Phase 5b: Fluvial aggradation and return to humid conditions

764 The following sub-phase, corresponding to unit U5b, is marked by a resumption of fluvial aggradation
765 within a more stable hydromorphic context. Flow conditions became more regular, favoring a rise in the
766 alluvial water table and sediment accumulation. Geochemical indicators reveal high organic matter
767 content (up to 30%), low carbonate concentration, predominance of fine particles, and a low Rb/Sr ratio,
768 pointing to a temporary return to a humid, low-energy fluvial environment.

769 - Phase 5c: Major erosive episode and return to arid conditions

770 The last sub-phase, dated by OSL between 9 500–8 500 BP and corresponding to units U5c and U5d,
771 records a new episode of intense erosion, well preserved on both banks of the Wadi Akka. Grain-size
772 and geochemical data attest to this hydrological dynamic: a high proportion of coarse fractions (sands,
773 gravels > 80%), elevated D50 and D90 values, and an accentuated Zr/Rb ratio. These parameters reflect
774 a powerful fluvial dynamic in a high-energy environment. Similarly, low Rb/Sr ratios suggest limited
775 pedological alteration, while the low organic matter content indicates sedimentation dominated by
776 detrital minerogenic inputs, with minimal biological contribution. These features are typical of more
777 arid climatic conditions.

This phase marks the transition between the Early and Middle Holocene and reflects a major change in sedimentary dynamics and paleoenvironmental conditions. It remains poorly documented in most Maghrebian fluvial archives (Zielhofer et al., 2008; Depreux et al., 2021).This regional sedimentary hiatus appears to result from major hydro-geomorphological disturbances affecting Moroccan fluvial systems, probably in response to two Rapid Climate Change (RCC) events that occurred around 8 200 and 7 600 cal BP in the Charef basin, a tributary of the lower Moulouya (Depreux et al., 2022)

Phase 6, dated between 8 500 and 7 204 cal BP corresponds to sedimentary unit U6, and is characterized by a new phase of erosion (Figure 9), followed by a thin alluvial aggradation (less than one meter). This sequence reflects a significant decrease in sedimentation rate, suggesting a reduction in fluvial dynamics, marking an environment of low fluvial activity.

Around 7 204 cal BP, Phase 7 (U7 and U8) begins with renewed aggradation in the alluvial plain (Figure 9), with deposits thicknesses ranging from 1 to 1.5 meters. This period records an energy shift, marked by an increase in coarse fractions and indices of aeolian contributions. These observations suggest a return to arid conditions in the region, with an environment increasingly influenced by wind action.

At regional and continental scales, this phase coincides with a period of progressive aridification, well documented in many paleoenvironmental archives. In particular, data from Lake Yoa, located in the heart of the central Sahara (Chad), reveal irregular declines in lake level beginning around 7 000 cal BP, reflecting a transition to more arid landscapes. These changes are generally attributed to modifications in North Atlantic atmospheric dynamics, notably a weakening or reorganization of the Atlantic Meridional Overturning Circulation (AMOC). This phenomenon likely disrupted rainfall regimes across North Africa, contributing to the progressive drying of Sahelo-Saharan wetlands (Sylvestre et al., 2024).

Following this phase, a long sedimentary hiatus is evident from geomorphological and especially geochronological data of the Akka river archive. This hiatus, extending from about 7 204 to 656 cal BP, suggests a period of hydrodynamic instability in the Wadi Akka, marked by incision and truncation, probably caused by one or several successive arid episodes. Such interruptions are frequently observed in African fluvial deposits and are often attributed to a decline in fluvial activity at the end of the African Humid Period (AHP) (Lespez et al., 2011; Depreux et al., 2021). Meanwhile, Sahelian and Sudanian regions experienced increasing aridity between about 5 000 and 3 000 cal BP (Demenocal et al., 2000; Lézine et al., 2005; Gasse, 2000), leading to the southward shift of major vegetation zones toward their modern limits. This climatic drought phase also corresponds to the intensification of aeolian processes, particularly in the Inner Niger Delta and its surroundings (Makaske, 1998), which probably caused the erosion of the rare wetter fluvial records of the Late Holocene, identified elsewhere in the upstream basin of the Drâa (Saadi et al., 2024). In the Maghreb, this transition is reflected by increased episodes

of torrential runoff and alluvial crises, indicating progressive regional aridification (Faust et al., 2004; Weisrock et al., 2006; Saadi et al., 2024).

5.6 Late Holocene / Little Ice Age

This interval marks a significant change in the sedimentation regime, following a long sedimentary hiatus in the Akka plain archives.

Phase 8, dated between 656 and 597 cal BP, is characterized by marked fluvial aggradation, reaching about 1 meter in thickness. This sequence reflects arid environmental conditions, evidenced by a high content of detrital elements (Zr, Si) (fig. x), low organic matter concentration, and a notable decrease in carbonates. These indicators suggest a lowering of the water table. Furthermore, a significant increase in magnetic susceptibility (MS), from 9×10^{-8} to 50×10^{-8} m^3/kg, indicates a change in sediment provenance, probably linked to a modification in sediment supply sources.

Phase 9, postdating 597 cal BP, is represented by unit U9c. It is expressed by a tufa formation containing travertine tubes, developed over alluvial deposits at higher elevation on the right bank of the Wadi Akka (Figure 6b). This phase is also marked by the development of a stromatolitic carbonate formation (Figure 6c), indicating a prolonged period of water abundance and stagnation. This phase, probably dated to the last five centuries, may correspond to one of the humid periods of the Little Ice Age (LIA), well documented in Moroccan regional archives. For example, increased humidity is recorded around 150–300 cal BP in the Ifoulki stalagmite (Middle Atlas; Ait Brahim et al., 2017),and between 300–400 cal BP in the tufa deposits of Imouzzer Kandar (Azennoud et al., 2022).

In North Africa, particularly in Saharan and pre-Saharan regions, paleoenvironmental data for the Late Holocene remain scarce, especially in alluvial archives. A recent comprehensive study by Saadi et al. (2024) in the middle basin of the Wadi Drâa has begun to fill this gap by integrating paleoenvironmental, paleohydrological, and archaeological archives. Their work provides an initial chronological framework for the main morphodynamic and paleoenvironmental phases documented over the last 3,500 years (cal BP).

Most of the environmental and climatic changes recorded in fluvial system archives have often been primarily attributed to human activities, with many studies emphasizing anthropogenic influences on geomorphological processes during the Late Holocene (Ramrath et al., 2000; Oldfield et al., 2003). However, the Holocene sedimentary archives of the Akka plain, located in a sub-Saharan region particularly sensitive to climatic fluctuations, indicate that the main environmental changes in this area are closely linked to major climatic events. The chronological and sedimentary hiatuses observed during the second half of the Middle Holocene and throughout the Late Holocene in the Wadi Akka archives correspond to phases of sediment truncation and intense hydro-sedimentary instability in the floodplain.

These episodes reflect a morphodynamic and hydrological context characterized by periods of severe erosion and substantial destruction of earlier sedimentary deposits.

6. Conclusion :

The sedimentary archives of the Akka alluvial plain provide a valuable new reference for understanding the impacts of climate change on the continental Saharan environment of North Africa during the Late Pleistocene to Holocene. This study focuses particularly on MIS 5b, MIS 3, and the Early Holocene period associated with the African Humid Period (AHP). Employing a multidisciplinary approach—including geomorphological and sedimentological field analyses, radiocarbon and OSL dating, and geochemical investigations—four alluvial sequences from the Akka plain, a right-bank tributary of the Drâa River in southern Morocco, were examined. This research enabled the reconstruction of environmental and morpho-hydrosedimentary conditions over five distinct phases, spanning more than 82,900 years, thereby providing new insights into the climatic and hydrological dynamics of the region.

- Around 82.9 ka (MIS 5b), the Akka plain underwent a phase of high-energy braided fluvial activity, marked by coarse gravel deposition and significant lateral instability, under a humid climatic regime associated with the end of the last interglacial..
- During MIS 3 (~40.5 ± 2.4 ka), fine-grained aggradation occurred under low-energy hydrological conditions, supported by geochemical proxies (e.g., high Rb/Sr ratios, organic-rich horizons), reflecting enhanced soil development and relatively humid conditions.40.5 ± 2.4 ka.
- Between 11,428 and 10,260 cal BP, a phase of silty aggradation marks the early African Humid Period (AHP) in the wadi Akka alluvial records, indicating humid conditions with low hydrodynamic energy.
- Between 10,260 and 9,500 cal BP, the persistence of humid and stable conditions is evidenced by tufa and peat accumulation, and the presence of aquatic fauna (e.g., *Melanopsis*), suggesting perennial freshwater environments and regional landscape stability.Between9 500 to 8500 cal BP, the system shifted toward a more dynamic regime, marked by torrential flows, coarse sediment input, and aeolian contributions, revealing a phase of increased climatic variability and sedimentary instability within the AHP.
- A return to wetter conditions is suggested around 7 204 cal BP, evidenced by silty aggradation and tufa facies, following a poorly documented but morphodynamically active interval dominated by incision and erosion.The most recent period, between 656 and 579 cal BP, signals a significant change in sedimentation consistent with arid conditions. However, after 597 cal BP, a wet phase is recorded, marked by large travertine tubes and stromatolithic travertine dams. This phase likely corresponds to the

879 last humid episode of the Little Ice Age (LIA), also associated with paleosol formation
880 in the middle Drâa Basin (Saadi et al., 2024)

881 At Akka, the fluvial record predominantly preserves the most humid phases of the Late Pleistocene and
882 Holocene, leading to an over-representation of wetter conditions in the sedimentary archive. In contrast,
883 the Middle Holocene and much of the Late Holocene are characterized by incision and truncation events,
884 often accompanied by gravel deposits resulting from highly erosive fluvial processes. These dynamics
885 account for the frequent sedimentary hiatuses and discontinuities observed in the fluvial systems. Such
886 periods appear to be linked to rapid climatic fluctuations and a general trend of aridification driven by
887 orbital forcing. Nevertheless, this extended interval remains poorly constrained chronologically at Akka
888 and will require substantial future efforts in geochronology, particularly through OSL dating, contingent
889 upon achieving sufficient bleaching of the alluvial deposits under study.

890 **Acknowledgments**

891 This study was carried out as part of the PHC Toubkal/21/132 project (Campus France) 45924WJ, as
892 well as the APPI-Lyon2 "Transmar" project. We would like to express our gratitude to the editor and
893 reviewers for their very helpful comments and suggestions. We also thank the Poznań Radiocarbon
894 Laboratory. We are grateful to the OMEAA platform (UMR 5600 EVS and 5133 Archéorient, University
895 of Lyon) for providing access to the facilities necessary for sample processing, and to the IRG/EVS team
896 for their financial support. We also extend our thanks to E. Rafins and M. Payet for preparing the
897 luminescence (OSL) samples.

898 **Figure legends:**

List of tables :

Supplementary Materials :

Methodology

1. Chronology

1.1 Optically Stimulated Luminescence (OSL) and post-Infrared Infrared Stimulated Luminescence (pIRIR290) Dating

OSL and pIRIR290 are trapped charge dating methods that allow dating the last bleaching event, i.e., the last exposure to light of quartz (OSL) and feldspar (pIRIR290) grains before deposition in a sedimentary layer (see details in Aitken, 1998). Both quartz and feldspars are able to record a dose of ionising rays coming from the sedimentary environment of the sample (from the decay of isotopes from the uranium, U, and thorium, Th, decay chains, as well as potassium, K), and the cosmic rays. The dose stored in the mineral is called the equivalent dose (De, in Gray, Gy) and is obtained by stimulating with light the sample, which will in turn emit light (the luminescence signal). To obtain the De, a dose response curve (DRC) is constructed by meas-uring the natural luminescence signal on an aliquot of a given sample, and regenerating this signal by irradiating the same aliquot at increasing doses using the single-aliquot regenerative-dose protocol (SAR, Murray & Wintle, 2000) The De is ob-tained by interpolation on the DRC. The age is obtained by dividing the De by the dose rate (Da, in Gy·a-1), i.e., the dose of radi-ation emitted per year in the surrounding of the sample and the sample itself (applicable for feldspars) and that corresponds to the sum of alpha, beta, and gamma rays, with the contribution of the cosmic rays. Three protocols were used in this study. First, the OSL SAR protocol was applied to quartz from multi-grain aliquots (Tab. S1). Considering that the OSL signal of sam-ple AKKA2-OSL1 was close to saturation, the pIRIR290 SAR protocol was applied to K-feldspars from multi-grain aliquots for this sample (Tab. S2). For the three other samples, OSL multigrain analyses showed that some aliquots were saturated or close to saturation, and/or high OD values were obtained (see details in the main text). We thus performed OSL single grain analyses on quartz from samples AKKA2-OSL2, 3 and 4 (Tab. S3).

Tab. S1. OSL SAR protocol applied to quartz from multi-grain aliquots.

Step	Treatment
1	Given dose
2	Preheat (240°C for 10 s)
3 (Lx)	Green stimulation for 100 s at 125°C
4	Given test dose
5	Cutheat (200°C for 0 s)

	6 (Tx)	Green stimulation for 100 s at 125°C
	7	Return to 1

998

999 *Tab. S2. $pIRIR_{290}$ SAR protocol applied to feldspars from multi-grain aliquots.*

Step	Treatment
1	Given dose
2	Preheat (320°C for 60 s)
3	Infrared stimulation for 200 s at 50°C
4 (Lx)	Infrared stimulation for 200 s at 290°C
5	Given test dose
6	Preheat (320°C for 60 s)
7	Infrared stimulation for 200 s at 50°C
8 (Tx)	Infrared stimulation for 200 s at 290°C
9	Optical draining (infrared stimulation for 100 s at 325°C)
10	Return to 1

1000

1001 *Tab. S3. OSL SG SAR protocol applied to quartz.*

Step	Treatment
1	Given dose (for N, dose = 0)
2	Preheat at 240°C for 10 s
3 (L_x)	SG Green stimulation at 125°C for 1s
4	Given test dose
5	Cutheat at 200°C for 0 s
6 (T_x)	SG Green stimulation at 125°C for 1s
7	Return to 1

1002 *Table S4. Statistics on the selected single grains. [1]Total number of individual quartz grains measured using the*
1003 *SAR protocol; [2]Number of grains that provided a luminescence signal passing the selection criteria; [3]Among the*
1004 *grains that passed criteria, those for which no intersection was reached, those for which the L_n/T_n signal was*
1005 *higher than the highest regenerated point (extrapolated grains), those for which the D_e was higher than two*
1006 *times D_0* (Wintle & Murray, 2006) *and those for which a $D_e < 0$ was obtained.*

	OSL2	OSL3	OSL4
Number of grains measured[1]	1000	1000	1000
Number of grains that passed criteria[2]	63	21	21
Number of rejected grains[3]	37	4	5
- No intersection	20	1	2
- Extrapolated grains	0	1	0

- Saturated grains ($D_e > 2*D_0$)	17	1	3
- Negative D_e	0	1	0
Accepted grains[4]	26	17	16

Principal Component Analysis (PCA)

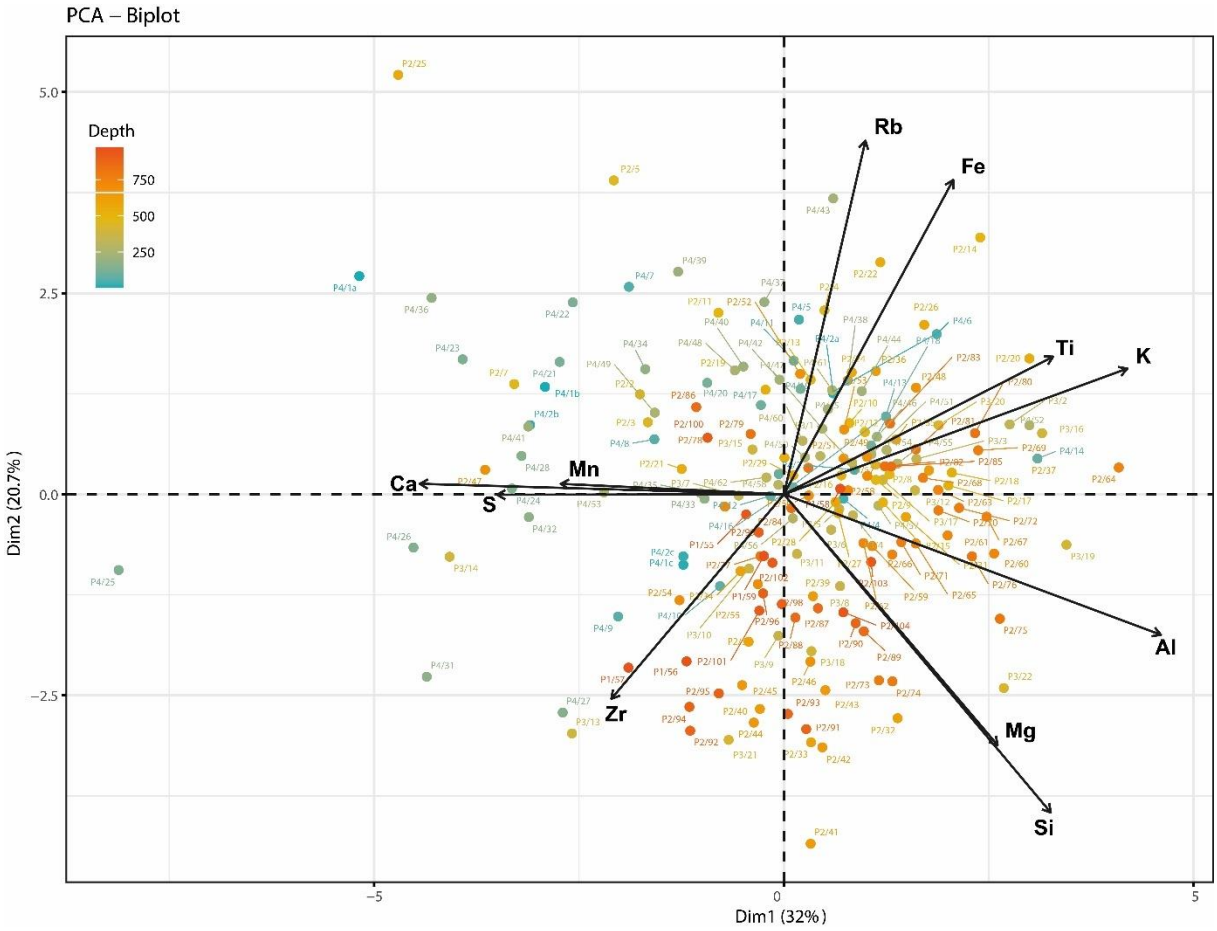

Figure 11 : *Results of the Principal Component Analysis (PCA) with the set of elements (samples)*

Références bibliographiques

Ait Brahim, Y., Seif-Ennasr, M., Malki, M., N'da, B., Choukrallah, R., El Morjani, Z. E. A., Sifeddine, A., Abahous, H., & Bouchaou, L. (2017). Assessment of climate and land use changes: Impacts on groundwater resources in the Souss-Massa River basin. *The Souss-Massa River Basin, Morocco*, 121–142.

Ait Brahim, Y., Wassenburg, J. A., Sha, L., Cruz, F. W., Deininger, M., Sifeddine, A., Bouchaou, L., Spötl, C., Edwards, R. L., & Cheng, H. (2019). North Atlantic ice-rafting, ocean and atmospheric circulation during the Holocene: Insights from Western Mediterranean speleothems. *Geophysical Research Letters*, *46*(13), 7614–7623.

Aitken, M. J. (1998). An introduction to optical dating: Oxford University Press. *New York*.

Azennoud, K., Baali, A., Brahim, Y. A., Ahouach, Y., & Hakam, O. (2022). Climate controls on tufa deposition over the last 5000 years: A case study from Northwest Africa. *Palaeogeography, Palaeoclimatology, Palaeoecology*, *586*, 110767.

Baqloul, A., Schefuß, E., Kölling, M., Dupont, L., Groeneveld, J., Zhao, X., Reddad, H., Bouchaou, L., & Bouimetarhan, I. (2021). Climate and land-use effects on hydrological and vegetation signals during the last three millennia: Evidence from sedimentary leaf waxes in southwestern Morocco. *The Holocene*, *31*(5), 699–708.

Bartz, M., Rixhon, G., Duval, M., Arnold, L. J., Demuro, M., King, G., Álvarez-Posada, C., Parés, J. M., & Brückner, H. (2018). *Une approche multi-méthodes originale: l'utilisation combinée de la résonance de spin électronique, de la luminescence et du paléomagnétisme pour reconstituer l'évolution quaternaire de la basse Moulouya (NE du Maroc)*.

Bereiter, B., Lüthi, D., Siegrist, M., Schüpbach, S., Stocker, T. F., & Fischer, H. (2012). Mode change of millennial CO2 variability during the last glacial cycle associated with a bipolar marine carbon seesaw. *Proceedings of the National Academy of Sciences*, *109*(25), 9755–9760.

Berger, A., & Loutre, M.-F. (1991). Insolation values for the climate of the last 10 million years. *Quaternary Science Reviews*, *10*(4), 297–317.

Berger, J.-F., Delhon, C., Magnin, F., Bonte, S., Peyric, D., Thiebault, S., Guilbert, R., & Beeching, A. (2016). A fluvial record of the mid-Holocene rapid climatic changes in the middle Rhone valley (Espeluche-Lalo, France) and of their impact on Late Mesolithic and Early Neolithic societies. *Quaternary Science Reviews*, *136*, 66–84.

Blott, S. J., & Pye, K. (2001). Graditat: a grain size distribution and statistics package for the analysis of unconsolidated sediments. *Earth Surface Processes and Landforms*, *26*(11), 1237–1248.

Bond, G., Kromer, B., Beer, J., Muscheler, R., Evans, M. N., Showers, W., Hoffmann, S., Lotti-Bond, R., Hajdas, I., & Bonani, G. (2001). Persistent solar influence on North Atlantic climate during the Holocene. *Science*, *294*(5549), 2130–2136.

Boudad, L., Kabiri, L., Weisrock, A., Wengler, L., Fontugne, M., El Maataoui, M., Makayssi, A., & Vernet, J. L. (2003). Les formations fluviatiles du Pléistocène supérieur et de l'Holocène dans la" plaine" de Tazoughmit (Oued Rheris, piémont sud-atlasique de Goulmina, Maroc)[Upper Pleistocene and Holocene fluvial sedimentation in the" pkaa" Tazoughmit (Oued Rheris, High At. *Quaternaire*, *14*(3), 139–154.

Brahim, Y. A., Cheng, H., Sifeddine, A., Wassenburg, J. A., Cruz, F. W., Khodri, M., Sha, L., Pérez-Zanón, N., Beraaouz, E. H., & Apaéstegui, J. (2017). Speleothem records decadal to multidecadal hydroclimate variations in southwestern Morocco during the last millennium. *Earth and Planetary Science Letters*, *476*, 1–10.

Brahim, Y. A., Sha, L., Wassenburg, J. A., Azennoud, K., Cheng, H., Cruz, F. W., & Bouchaou, L. (2023). The spatiotemporal extent of the Green Sahara during the last glacial period. *Iscience*, *26*(7).

Bravard, J.-P. (1983). Les sédiments fins des plaines d'inondation dans la vallée du Haut-Rhône. *Revue de Géographie Alpine*, *71*(4), 363–379.

Brennan, B. J., Lyons, R. G., & Phillips, S. W. (1991). Attenuation of alpha particle track dose for spherical grains. *International Journal of Radiation Applications and Instrumentation. Part D. Nuclear Tracks and Radiation Measurements*, *18*(1–2), 249–253.

Burrough, S. L., & Thomas, D. S. G. (2013). Central southern Africa at the time of the African Humid Period: a new analysis of Holocene palaeoenvironmental and palaeoclimate data. *Quaternary Science Reviews*, *80*, 29–46.

Campbell, J. F. E., Fletcher, W. J., Joannin, S., Hughes, P. D., Rhanem, M., & Zielhofer, C. (2017). Environmental drivers of Holocene forest development in the Middle Atlas, Morocco. *Frontiers in Ecology and Evolution*, *5*, 113.

Castañeda, I. S., Mulitza, S., Schefuß, E., Lopes dos Santos, R. A., Sinninghe Damsté, J. S., & Schouten, S. (2009). Wet phases in the Sahara/Sahel region and human migration patterns in North Africa. *Proceedings of the National Academy of Sciences*, *106*(48), 20159–20163.

Cheddadi, R., Carré, M., Nourelbait, M., François, L., Rhoujjati, A., Manay, R., Ochoa, D., & Schefuss, E.

(2021). Early Holocene greening of the Sahara requires Mediterranean winter rainfall. *Proceedings of the National Academy of Sciences*, *118*(23), e2024898118.

Cheddadi, R., Fady, B., François, L., Hajar, L., Suc, J., Huang, K., Demarteau, M., Vendramin, G. G., & Ortu, E. (2009). Putative glacial refugia of Cedrus atlantica deduced from Quaternary pollen records and modern genetic diversity. *Journal of Biogeography*, *36*(7), 1361–1371.

Chennaoui, K., Nahid, A., Argant, J., Noçairi, M., Malek, F., & Sahbi, H. (2005). Etude intégrée d'un enregistrement morphosédimentaire anthropique holocène: l'escargotière de Tissouirine (Atlas atlantique, Maroc). *Revue de Paléobiologie*, *24*(2), 541–550.

Choubert, G., & Ennadifi, Y. (1970). *Carte géologique du flanc sud de l'Anti-Atlas Occidental et des Plaines du Dra: Akka-Tafagount-Tata*. Service géologique du Maroc.

Cremaschi, M., & Zerboni, A. (2011). Human communities in a drying landscape: Holocene climate change and cultural response in the central Sahara. *Landscapes and Societies: Selected Cases*, 67–89.

Cremaschi, M., Zerboni, A., Mercuri, A. M., Olmi, L., Biagetti, S., & Di Lernia, S. (2014). Takarkori rock shelter (SW Libya): an archive of Holocene climate and environmental changes in the central Sahara. *Quaternary Science Reviews*, *101*, 36–60.

Cremaschi, M., Zerboni, A., Spötl, C., & Felletti, F. (2010). The calcareous tufa in the Tadrart Acacus Mt.(SW Fezzan, Libya): an early Holocene palaeoclimate archive in the central Sahara. *Palaeogeography, Palaeoclimatology, Palaeoecology*, *287*(1–4), 81–94.

Dearing, J. (1999). Magnetic susceptibility. *Environmental Magnetism: A Practical Guide*, 35–62.

DeMenocal, P. B., & Tierney, J. E. (2012). Green Sahara: African humid periods paced by Earth's orbital changes. *Nature Education Knowledge*, *3*(10), 12.

Demenocal, P., Ortiz, J., Guilderson, T., Adkins, J., Sarnthein, M., Baker, L., & Yarusinsky, M. (2000). Abrupt onset and termination of the African Humid Period:: rapid climate responses to gradual insolation forcing. *Quaternary Science Reviews*, *19*(1–5), 347–361.

Depreux, B. (2021). *Dynamiques des systèmes fluviaux dans le bassin de la Moulouya (Maroc) à l'Holocène: morphogenèse fluviale, changements climatiques et occupations humaines*. Montpellier 3.

Depreux, B., Berger, J.-F., Lefèvre, D., Wackenheim, Q., Andrieu-Ponel, V., Vinai, S., Degeai, J.-P., El Harradji, A., Boudad, L., & Sanz-Laliberté, S. (2022). First fluvial archive of the 8.2 and 7.6–7.3 ka events in North Africa (Charef River, High Plateaus, NE Morocco). *Scientific Reports*, *12*(1), 7710.

Depreux, B., Lefèvre, D., Berger, J.-F., Segaoui, F., Boudad, L., El Harradji, A., Degeai, J.-P., & Limondin-Lozouet, N. (2021). Alluvial records of the African Humid Period from the NW African highlands (Moulouya basin, NE Morocco). *Quaternary Science Reviews*, *255*, 106807.

El Amrani, M., Macaire, J.-J., Zarki, H., Bréhéret, J.-G., & Fontugne, M. (2008). Contrasted morphosedimentary activity of the lower Kert River (northeastern Morocco) during the Late Pleistocene and the Holocene. Possible impact of bioclimatic variations and human action. *Comptes Rendus. Géoscience*, *340*(8), 533–542.

Faust, D., Zielhofer, C., Escudero, R. B., & del Olmo, F. D. (2004). High-resolution fluvial record of late Holocene geomorphic change in northern Tunisia: climatic or human impact? *Quaternary Science Reviews*, *23*(16–17), 1757–1775.

Fleitmann, D., Burns, S. J., Mangini, A., Mudelsee, M., Kramers, J., Villa, I., Neff, U., Al-Subbary, A. A., Buettner, A., & Hippler, D. (2007). Holocene ITCZ and Indian monsoon dynamics recorded in stalagmites from Oman and Yemen (Socotra). *Quaternary Science Reviews*, *26*(1–2), 170–188.

Fletcher, W. J., Debret, M., & Goñi, M. F. S. (2013). Mid-Holocene emergence of a low-frequency millennial oscillation in western Mediterranean climate: Implications for past dynamics of the North Atlantic atmospheric westerlies. *The Holocene*, *23*(2), 153–166.

Foley, J. A., Coe, M. T., Scheffer, M., & Wang, G. (2003). Regime shifts in the Sahara and Sahel: interactions

between ecological and climatic systems in Northern Africa. *Ecosystems*, *6*(6), 524–532.

Fontes, J. C., Gasse, F., Callot, Y., Plaziat, J. C., Carbonel, P., Dupeuble, P. A., & Kaczmarska, I. (1985). Freshwater to marine-like environments from Holocene lakes in northern Sahara. *Nature*, *317*(6038), 608–610.

Galbraith, R. F., Roberts, R. G., Laslett, G. M., Yoshida, H., & Olley, J. M. (1999). Optical dating of single and multiple grains of quartz from Jinmium rock shelter, northern Australia: Part I, experimental design and statistical models. *Archaeometry*, *41*(2), 339–364.

Gasse, F. (2000). Hydrological changes in the African tropics since the Last Glacial Maximum. *Quaternary Science Reviews*, *19*(1–5), 189–211.

Gasse, F. (2002). Diatom-inferred salinity and carbonate oxygen isotopes in Holocene waterbodies of the western Sahara and Sahel (Africa). *Quaternary Science Reviews*, *21*(7), 737–767.

Gasse, F., Téhet, R., Durand, A., Gibert, E., & Fontes, J.-C. (1990). The arid–humid transition in the Sahara and the Sahel during the last deglaciation. *Nature*, *346*(6280), 141–146.

Guérin, G., Mercier, N., & Adamiec, G. (2011). Dose-rate conversion factors: update. *Ancient Tl*, *29*(1), 5–8.

Guérin, G., Mercier, N., Nathan, R., Adamiec, G., & Lefrais, Y. (2012). On the use of the infinite matrix assumption and associated concepts: a critical review. *Radiation Measurements*, *47*(9), 778–785.

Haslett, S. K., & Smart, C. W. (2006). Late Quaternary upwelling off tropical NW Africa: new micropalaeontological evidence from ODP Hole 658C. *Journal of Quaternary Science: Published for the Quaternary Research Association*, *21*(3), 259–269.

Heiri, O., Lotter, A. F., & Lemcke, G. (2001). Loss on ignition as a method for estimating organic and carbonate content in sediments: reproducibility and comparability of results. *Journal of Paleolimnology*, *25*, 101–110.

Helmens, K. F. (2014). The Last Interglacial–Glacial cycle (MIS 5–2) re-examined based on long proxy records from central and northern Europe. *Quaternary Science Reviews*, *86*, 115–143.

Ibouhouten, H., Zielhofer, C., Mahjoubi, R., Kamel, S., Linstädter, J., Mikdad, A., Bussmann, J., Werner, P., Härtling, J. W., & Fenech, K. (2010). Archives alluviales holocènes et occupation humaine en Basse Moulouya (Maroc nord-oriental). *Géomorphologie: Relief, Processus, Environnement*, *16*(1), 41–56.

Jones, A. F., Macklin, M. G., & Brewer, P. A. (2012). A geochemical record of flooding on the upper River Severn, UK, during the last 3750 years. *Geomorphology*, *179*, 89–105.

Klasen, N., Fischer, P., Lehmkuhl, F., & Hilgers, A. (2015). Luminescence dating of loess deposits from the Remagen-Schwalbenberg site, Western Germany. *Geochronometria*, *42*(1).

Kröpelin, S., Verschuren, D., Lézine, A.-M., Eggermont, H., Cocquyt, C., Francus, P., Cazet, J.-P., Fagot, M., Rumes, B., & Russell, J. M. (2008). Climate-driven ecosystem succession in the Sahara: the past 6000 years. *Science*, *320*(5877), 765–768.

Kutzbach, J. E. (1981). Monsoon climate of the early Holocene: climate experiment with the earth's orbital parameters for 9000 years ago. *Science*, *214*(4516), 59–61.

Lauterbach, S., Brauer, A., Andersen, N., Danielopol, D. L., Dulski, P., Hüls, M., Milecka, K., Namiotko, T., Obremska, M., & Von Grafenstein, U. (2011). Environmental responses to Lateglacial climatic fluctuations recorded in the sediments of pre-Alpine Lake Mondsee (northeastern Alps). *Journal of Quaternary Science*, *26*(3), 253–267.

Lefèvre, D. (1985). *Les formations plio-pléistocènes du bassin de Ksabi (Moyenne Moulouya, Maroc)*. Bordeaux 1.

Lespez, L., Le Drezen, Y., Garnier, A., Rasse, M., Eichhorn, B., Ozainne, S., Ballouche, A., Neumann, K., & Huysecom, E. (2011). High-resolution fluvial records of Holocene environmental changes in the Sahel: the Yamé River at Ounjougou (Mali, West Africa). *Quaternary Science Reviews*, *30*(5–6), 737–756.

Lézine, A.-M., & Casanova, J. (1989). Pollen and hydrological evidence for the interpretation of past climates in tropical West Africa during the Holocene. *Quaternary Science Reviews*, *8*(1), 45–55.

Lézine, A.-M., Duplessy, J.-C., & Cazet, J.-P. (2005). West African monsoon variability during the last deglaciation and the Holocene: Evidence from fresh water algae, pollen and isotope data from core KW31, Gulf of Guinea. *Palaeogeography, Palaeoclimatology, Palaeoecology*, *219*(3–4), 225–237.

Lézine, A.-M., Hély, C., Grenier, C., Braconnot, P., & Krinner, G. (2011). Sahara and Sahel vulnerability to climate changes, lessons from Holocene hydrological data. *Quaternary Science Reviews*, *30*(21–22), 3001–3012.

Lézine, A.-M., Kageyama, M., & Bassinot, F. (2023). Data and models reveal humid environmental conditions during MIS 3 in two of the world's largest deserts. *Comptes Rendus. Géoscience*, *355*(S2), 229–246.

Lézine, A.-M., Saliege, J.-F., Robert, C., Wertz, F., & Inizan, M.-L. (1998). Holocene lakes from Ramlat as-Sab'atayn (Yemen) illustrate the impact of monsoon activity in southern Arabia. *Quaternary Research*, *50*(3), 290–299.

Lghamour, M., Karrat, L., Picotti, V., Hajdas, I., Haghipour, N., Guidobaldi, G., Heeb, K. W., & Gourari, L. (2024). Late Pleistocene to Holocene alluvial deposits of the Inaouène Valley and their paleoenvironmental significance (north Morocco). *Quaternary Science Reviews*, *344*, 108941.

Liang, L., Sun, Y., Beets, C. J., Prins, M. A., Wu, F., & Vandenberghe, J. (2013). Impacts of grain size sorting and chemical weathering on the geochemistry of Jingyuan loess in the northwestern Chinese Loess Plateau. *Journal of Asian Earth Sciences*, *69*, 177–184.

Limondin-Lozouet, N., Haddoumi, H., Lefèvre, D., Ghamizi, M., Aouraghe, H., & Salel, T. (2013). Holocene molluscan succession from NE Morocco: Palaeoenvironmental reconstruction and biogeographical implications. *Quaternary International*, *302*, 61–76.

Linnaeus, C. (1789). *Systema Naturae per regna tria naturae, secundum classes, ordines, genera, species; cum characteribus, differentiis, synonymis, locis* (Vol. 1). apud JB Delamolliere.

Makaske, B. (1998). *Anastomosing rivers: forms, processes and sediments* (Issue 249).

Maley, J., & Vernet, R. (2013). Peuples et évolution climatique en Afrique nord-tropicale, de la fin du Néolithique à l'aube de l'époque moderne. *Afriques. Débats, Méthodes et Terrains d'histoire*, *04*.

Mathieu, J., Weisrock, A., Wengler, L., Brochier, J. E., Even, G., Fontugne, M., Mercier, N., Ouammou, A., Senegas, F., & Valladas, H. (2004). Holocene deposits in the lower section of the Assaka wadi, South Morocco: Preliminary results. *Quaternaire*, *15*(1–2), 207–218.

Mercier, N., & Falguères, C. (2007). Field gamma dose-rate measurement with a NaI (Tl) detector: re-evaluation of the" threshold" technique. *Ancient TL*, *25*(1), 1–4.

Mullins, C. E. (1977). Magnetic susceptibility of the soil and its significance in soil science–a review. *Journal of Soil Science*, *28*(2), 223–246.

Murray, A. S., & Wintle, A. G. (2000). Luminescence dating of quartz using an improved single-aliquot regenerative-dose protocol. *Radiation Measurements*, *32*(1), 57–73.

Ndiaye, A., Bentaleb, I., Favier, C., Fourel, F., Sebag, D., Fall, M., Giresse, P., & Diouf, B. (2022). Reconstruction of the holocene climate and environmental changes of Niayes peat bog in northern coast of Senegal (NW Africa) based on stable isotopes and charcoals analysis. *Quaternary Science Reviews*, *289*, 107609.

Oldfield, F., Asioli, A., Accorsi, C. A., Mercuri, A. M., Juggins, S., Langone, L., Rolph, T., Trincardi, F., Wolff, G., & Gibbs, Z. (2003). A high resolution late Holocene palaeo environmental record from the central Adriatic Sea. *Quaternary Science Reviews*, *22*(2–4), 319–342.

Ouammou, A. (1993). *Evolution morphologique récente du bas plateau de Tiznit (Maroc)*. Nancy 2.

Pachur, H-J, Röper, H.-P., Kroepelin, S., & Goschin, M. (1987). *Late Quaternary hydrography of the eastern*

Sahara.

Pachur, Hans-Joachim, & Hoelzmann, P. (1991). Paleoclimatic implications of late Quaternary lacustrine sediments in western Nubia, Sudan. *Quaternary Research*, *36*(3), 257–276.

Paine, A. R., Baldini, J. U. L., Ünal-Imer, E., Wadsworth, F. B., Iveson, A. A., Humphreys, M. C. S., Brown, R. J., Müller, W., & Ottley, C. J. (2024). Abrupt climate change at the MIS 5/4 transition recorded in a speleothem from the Eastern Mediterranean. *Quaternary Science Reviews*, *339*, 108841.

Parker, A. O., Schmidt, M. W., Jobe, Z. R., & Slowey, N. C. (2016). A new perspective on West African hydroclimate during the last deglaciation. *Earth and Planetary Science Letters*, *449*, 79–88.

Passega, R. (1964). Grain size representation by CM patterns as a geologic tool. *Journal of Sedimentary Research*, *34*(4), 830–847.

Pausata, F. S. R., Gaetani, M., Messori, G., Berg, A., de Souza, D. M., Sage, R. F., & DeMenocal, P. B. (2020). The greening of the Sahara: Past changes and future implications. *One Earth*, *2*(3), 235–250.

Petit-Maire, N, & Riser, J. (1981). Holocene lake deposits and palaeoenvironments in central Sahara, northeastern Mali. *Palaeogeography, Palaeoclimatology, Palaeoecology*, *35*, 45–61.

Petit-Maire, N, Sanlaville, P., & YAN, Z. (1995). Oscillations de la limite nord du domaine des moussons africaine, indienne, et asiatique au cours du dernier cycle climatique. *Bulletin de La Société Géologique de France*, *166*(2), 213–220.

Petit-Maire, Nicole. (1989). Interglacial environments in presently hyperarid Sahara: palaeoclimatic implications. In *Paleoclimatology and Paleometeorology: modern and past patterns of global atmospheric transport* (pp. 637–661). Springer.

Petit-Maire, Nicole. (2021). *Sahara: les grands changements climatiques naturels*. Éditions Errance.

Petit-Maire, Nicole, & Riser, J. (1983). Sahara ou Sahel. *Quaternaire Récent Du Bassin de Taoudenni (Mali). Paris: Centre National de La Recherche Scientifique*, *473*.

Petit-Maire, Nicole, Riser, J., Blanc-Vernet, L., & Fairbridge, R. W. (1983). Sahara ou Sahel?: quaternaire récent du Bassin de Taoudenni (Mali). *(No Title)*.

Prescott, J. R., & Hutton, J. T. (1988). Cosmic ray and gamma ray dosimetry for TL and ESR. *International Journal of Radiation Applications and Instrumentation. Part D. Nuclear Tracks and Radiation Measurements*, *14*(1–2), 223–227.

Preusser, F., Radies, D., & Matter, A. (2002). A 160,000-year record of dune development and atmospheric circulation in Southern Arabia. *Science*, *296*(5575), 2018–2020.

Profe, J., Zolitschka, B., Schirmer, W., Frechen, M., & Ohlendorf, C. (2016). Geochemistry unravels MIS 3/2 paleoenvironmental dynamics at the loess–paleosol sequence Schwalbenberg II, Germany. *Palaeogeography, Palaeoclimatology, Palaeoecology*, *459*, 537–551.

Ramrath, A., Sadori, L., & Negendank, J. F. W. (2000). Sediments from Lago di Mezzano, central Italy: a record of Lateglacial/Holocene climatic variations and anthropogenic impact. *The Holocene*, *10*(1), 87–95.

Rasse, M., Lespez, L., Lebrun, B., Tribolo, C., Chevrier, B., Douze, K., Garnier, A., Davidoux, S., Hadjas, I., & Ollier, C. (2020). Synthèse morpho-sédimentaire et occurences archéologiques dans la vallée de la Falémé (de 80 à 5 ka; Sénégal oriental): mise en évidence d'une permanence des occupations à la transition Pléistocène-Holocène. *Quaternaire. Revue de l'Association Française Pour l'étude Du Quaternaire*, *31/1*, 71–88.

Reimer, P. J., Austin, W. E. N., Bard, E., Bayliss, A., Blackwell, P. G., Ramsey, C. B., Butzin, M., Cheng, H., Edwards, R. L., & Friedrich, M. (2020). The IntCal20 Northern Hemisphere radiocarbon age calibration curve (0–55 cal kBP). *Radiocarbon*, *62*(4), 725–757.

Renssen, H., Brovkin, V., Fichefet, T., & Goosse, H. (2003). Holocene climate instability during the termination of the African Humid Period. *Geophysical Research Letters*, *30*(4).

Richter, D., Richter, A., & Dornich, K. (2013). Lexsyg—A new system for luminescence research. *Geochronometria*, *40*(4), 220–228.

Richter, D., Richter, A., & Dornich, K. (2015). Lexsyg smart—a luminescence detection system for dosimetry, material research and dating application. *Geochronometria*, *42*(1), 202–209.

Ritchie, J. C., Eyles, C. H., & Haynes, C. V. (1985). Sediment and pollen evidence for an early to mid-Holocene humid period in the eastern Sahara. *Nature*, *314*(6009), 352–355.

Roberts, N., Brayshaw, D., Kuzucuoğlu, C., Perez, R., & Sadori, L. (2011). The mid-Holocene climatic transition in the Mediterranean: Causes and consequences. *The Holocene*, *21*(1), 3–13.

Romero, O. E., Leduc, G., Vidal, L., & Fischer, G. (2011). Millennial variability and long-term changes of the diatom production in the eastern equatorial Pacific during the last glacial cycle. *Paleoceanography*, *26*(2).

Rothwell, R. G., & Croudace, I. w. (2015). Twenty years of XRF core scanning marine sediments: What do geochemical proxies tell us? *Micro-XRF Studies of Sediment Cores: Applications of a Non-Destructive Tool for the Environmental Sciences*, 25–102.

Saadi, F., Boudad, L., & Berger, J.-F. (2024). Late Holocene morphosedimentary and palaeoenvironmental study of the Middle Drâa river basin (southeastern Morocco). *Quaternary International*.

Salvador, P.-G. (2016). Caractérisation des remblaiements sédimentaires de six paléochenaux de la plaine alluviale du Rhône par la méthode granulométrique de Passega (Basses Terres, Ain, Isère). *Bulletin de La Société Géographique de Liège*, *67*, 107–124.

Salzmann, U., & Waller, M. (1998). The Holocene vegetational history of the Nigerian Sahel based on multiple pollen profiles. *Review of Palaeobotany and Palynology*, *100*(1–2), 39–72.

Siddall, M., Stocker, T. F., Blunier, T., Spahni, R., McManus, J. F., & Bard, E. (2006). Using a maximum simplicity paleoclimate model to simulate millennial variability during the last four glacial periods. *Quaternary Science Reviews*, *25*(23–24), 3185–3197.

Specht, N. F., Claussen, M., & Kleinen, T. (2024). Dynamic interaction between lakes, climate, and vegetation across northern Africa during the mid-Holocene. *Climate of the Past*, *20*(7), 1595–1613.

Street-Perrott, F. A., Hales, P. E., Perrott, R. A., Fontes, J. C., Switsur, V. R., & Pearson, A. (1993). Late Quaternary palaeolimnology of a tropical marl lake: Wallywash Great Pond, Jamaica. *Journal of Paleolimnology*, *9*, 3–22.

Sylvestre, F., Melles, M., Wennrich, V., Dinies, M., Chalié, F., Swingedouw, D., Dallmeyer, A., Shi, X., Claussen, M., & Jaeschke, A. (2024). *Drought events during the African Humid Period suggest future drying of the Sahara*.

Tadoumant, S., Bouimetarhan, I., Baqloul, A., Hssaisoune, M., Reddad, H., & Bouchaou, L. (2022). Modern pollen distribution and its relationship with environmental gradient in southern Morocco. *Review of Palaeobotany and Palynology*, *298*, 104595.

Thiel, C., Buylaert, J.-P., Murray, A., Terhorst, B., Hofer, I., Tsukamoto, S., & Frechen, M. (2011). Luminescence dating of the Stratzing loess profile (Austria)–Testing the potential of an elevated temperature post-IR IRSL protocol. *Quaternary International*, *234*(1–2), 23–31.

Tribolo, C., Mercier, N., Douville, E., Joron, J.-L., Reyss, J.-L., Rufer, D., Cantin, N., Lefrais, Y., Miller, C. E., & Porraz, G. (2013). OSL and TL dating of the Middle Stone Age sequence at Diepkloof Rock Shelter (South Africa): a clarification. *Journal of Archaeological Science*, *40*(9), 3401–3411.

Wang, M., Zheng, H., Xie, X., Fan, D., Yang, S., Zhao, Q., & Wang, K. (2011). A 600-year flood history in the Yangtze River drainage: comparison between a subaqueous delta and historical records. *Chinese Science Bulletin*, *56*, 188–195.

Weisrock, A. L. E. (1980). *Géomorphologie et paléoenvironnements de l'Atlas atlantique (Maroc).* Université de Lille III, Atelier national de reproduction des thèses.

Weisrock, A, Ouammou, A., & Hssaine, A. (1991). Erosion et sédimentation dans les oueds du Sud-Ouest marocain à l'Holocène. *Géo Physio*, *22–23*, 95–100.

Weisrock, André, Rousseau, L., Reyss, J.-L., Falguères, C., Ghaleb, B., Bahain, J.-J., Beauchamp, J., Boudad, L., Mercier, N., & Mahieux, G. (2008). Travertins de la bordure nord du Sahara marocain: dispositifs morphologiques, datations U/Th et indications paléoclimatiques. *Géomorphologie: Relief, Processus, Environnement*, *14*(3), 153–167.

Weisrock, André, Wahl, L., Ouammou, A., & Chakir, L. (2006). Systèmes fluviaux du Sud-Ouest marocain et leur évolution depuis le Pléistocène supérieur. *Géomorphologie: Relief, Processus, Environnement*, *12*(4), 229–248.

Weldeab, S., Schneider, R. R., Kölling, M., & Wefer, G. (2005). Holocene African droughts relate to eastern equatorial Atlantic cooling. *Geology*, *33*(12), 981–984.

Wengler, L., Weisrock, A., Brochier, J.-É., Brugal, J. P., Fontugne, M., Magnin, F., Mathieu, J., Mercier, N., Ouammou, A., & Reyss, J.-L. (2002). Enregistrement fluviatile et paléoenvironnements au Pléistocène supérieur sur la bordure méridionale atlantique de l'Anti-Atlas (Oued Assaka, SO marocain). *Quaternaire*, *13*(3), 179–192.

Wintle, A. G., & Murray, A. S. (2006). A review of quartz optically stimulated luminescence characteristics and their relevance in single-aliquot regeneration dating protocols. *Radiation Measurements*, *41*(4), 369–391.

Yan, Z., & Petit-Maire, N. (1994). The last 140 ka in the Afro-Asian arid/semi-arid transitional zone. *Palaeogeography, Palaeoclimatology, Palaeoecology*, *110*(3–4), 217–233.

Zaky, A. S., de Azevedo, A. Q., Vogel, H., Jovane, L., Hamdan, M., Achyuthan, H., Frontalini, F., Szidat, S., & Anselmetti, F. S. (2024). Climate variability in northern Africa during the late Holocene: A multiproxy perspective from El-Beida Lake (Wadi El-Natrun, Egypt). *Quaternary Science Reviews*, *337*, 108801.

Zech, M., Zech, R., Zech, W., Glaser, B., Brodowski, S., & Amelung, W. (2008). Characterisation and palaeoclimate of a loess-like permafrost palaeosol sequence in NE Siberia. *Geoderma*, *143*(3–4), 281–295.

Zielhofer, C., Bussmann, J., Ibouhouten, H., & Fenech, K. (2010). Flood frequencies reveal Holocene rapid climate changes (Lower Moulouya River, northeastern Morocco). *Journal of Quaternary Science*, *25*(5), 700–714.

Zielhofer, C., & Faust, D. (2008). Mid-and Late Holocene fluvial chronology of Tunisia. *Quaternary Science Reviews*, *27*(5–6), 580–588.

Zielhofer, C., Faust, D., & Linstädter, J. (2008). Late Pleistocene and Holocene alluvial archives in the Southwestern Mediterranean: Changes in fluvial dynamics and past human response. *Quaternary International*, *181*(1), 39–54.